



1 **Riukojietna, a small low-altitude ice cap that may have persisted**  
2 **through the Holocene: Evidence from combining cosmogenic**  
3 **multi-nuclide dating and lacustrine sediment records**

4 Arjen P. Stroeven<sup>1,2</sup>, Gunhild C. Rosqvist<sup>1,2</sup>, Allie J. Koester<sup>3</sup>, Jane L. Andersen<sup>1,4</sup>, Carl-Anton  
5 Wahlström<sup>5</sup>, Nathaniel A. Lifton<sup>3,6</sup>

6 <sup>1</sup> Department of Physical Geography, Stockholm University, 106 91 Stockholm, Sweden

7 <sup>2</sup> Bolin Centre for Climate Research, Stockholm University, 106 91 Stockholm, Sweden

8 <sup>3</sup> Department of Earth, Atmospheric, and Planetary Sciences, Purdue University, West Lafayette IN 47907  
9 USA

10 <sup>4</sup> Research Centre for the Built Environment, Energy, Climate, and Water Technology, VIA University  
11 College, 8700 Horsens, Denmark

12 <sup>5</sup> IKNI AS, PO Box 6646, 0129 Oslo, Norway

13 <sup>6</sup> Purdue Rare Isotope Measurement Laboratory (PRIME Lab), Department of Physics and Astronomy,  
14 Purdue University, West Lafayette IN 47907, USA

15 *Correspondence to:* Arjen P. Stroeven (arjen.stroeven@natgeo.su.se)

16 **Abstract.** Riukojietna, a small, low-altitude, low-gradient plateau ice cap in northern Sweden, has been  
17 retreating rapidly over at least the last century. Its low surface gradient implies that it should be quite  
18 sensitive to, and therefore a potentially valuable indicator of, climate change since regional deglaciation at  
19 9.8 ka. Here, we assess its former extent and activity by combining cosmogenic nuclide measurements in  
20 bedrock (*in situ* <sup>14</sup>C, <sup>10</sup>Be, and <sup>26</sup>Al) that constrain ice-free and ice-buried conditions with indirect  
21 evidence of glacial activity from proglacial lake sediment records, complemented by historical ice  
22 thickness reconstructions. These data are the basis for subsequent forward modeling of measured  
23 cosmogenic nuclide concentrations to constrain the Holocene history of Riukojietna.

24 The ice cap has an outlet glacier tongue that drains to the northeast, with a bouldery moraine deposit  
25 further down valley constraining its extent at the end of the Little Ice Age (LIA, ca. 1910 CE). Five  
26 cosmogenic nuclide samples were collected: two from bedrock on the plateau adjacent to the ice cap, two  
27 from a bedrock knob protruding from the outlet glacier tongue (exposed in 2011), and one from an  
28 outcrop adjacent to the LIA moraine at the outlet of the most proximal of a series of four proglacial lakes.  
29 The latter sample yielded concentrations of <sup>14</sup>C, <sup>10</sup>Be, and <sup>26</sup>Al consistent with continuous exposure since  
30  $8.1 \pm 0.1$  ka (weighted mean). Nuclide measurements in the other four samples indicate complex  
31 exposure/burial histories. Lake cores from Pajep Luoktejaure, the third of the four down-valley proglacial  
32 lakes, indicate up to three periods of glacial sediment deposition since deglaciation, separated by  
33 gyttja, with radiocarbon age constraints from bulk sediment and plant macrofossils.



34 Modeled *in situ*  $^{14}\text{C}$  inventories for the two plateau samples are consistent with early Holocene ice cover,  
35 followed by exposure between  $8.1 \pm 0.1$  ka and the start of Riukojietna neoglacial expansion  $1.8 \pm 0.1$  ka  
36 ka BP, yet  $^{10}\text{Be}$  and  $^{26}\text{Al}$  concentrations are underestimated, indicating significant pre-Last Glacial  
37 Maximum exposure not considered in the modeling. Modeled *in situ*  $^{14}\text{C}$  concentrations of the samples  
38 from the emerging bedrock knob with this ice-cover history and a subglacial erosion rate of  $0.05 \text{ mm yr}^{-1}$   
39 are consistent with the measured values, while  $^{10}\text{Be}$  and  $^{26}\text{Al}$  concentrations again underestimate the  
40 measured values. Observed glacial laminated sediments in Pajep Luoktejaure between ca. 5.4-5.0 ka  
41 may indicate a brief readvance over the sampled cosmogenic nuclide sites, but agreement between  
42 modeled and measured *in situ*  $^{14}\text{C}$  values deteriorates slightly with that ice-cover interval. We use these  
43 results to infer that Riukojietna persisted during the Holocene Thermal Maximum (ca. 8-5 ka), in contrast  
44 to earlier suggestions that Scandinavian glaciers vanished during the Holocene, as a result of increased  
45 precipitation due to atmospheric circulation changes. The glacier has been in a retracted state similar or  
46 smaller than today during the late Holocene, as climate grew colder and drier. This approach combining  
47 short- and long-lived cosmogenic nuclides with lake sediments can thus provide new constraints on high-  
48 latitude Holocene glacial and paleoclimate history.

## 49 **1 Introduction and Background**

50 Mountain glaciers and ice caps are reliable indicators of regional climate change on decadal timescales  
51 because their mass balances are sensitive to changes in winter precipitation and summer ablation  
52 (Oerlemans and Fortuin, 1992; Oerlemans, 2005; Andreassen et al., 2020; Hugonnet et al., 2021; Rounce  
53 et al., 2023). Indeed, worldwide, glaciers have retreated at accelerating rates during the 20<sup>th</sup> century  
54 (Dussaillant et al., 2025; WGMS, 2025) and are projected for continued decline throughout the 21<sup>st</sup> century  
55 due to increased global temperatures (Oerlemans et al., 1998; Hock et al., 2019). Within this observed  
56 contemporary framework, this study explores the response of a small low-altitude Swedish ice cap,  
57 Riukojietna, to Holocene climate change.

58 A direct method to reconstruct the former extent of a glacier or ice sheet relies on exposure dating with  
59 cosmogenic nuclides in bedrock or erratics (e.g., Dunai, 2010). In glacial landscapes, the inventory of  
60 cosmogenic nuclides such as  $^{10}\text{Be}$  ( $t_{1/2} = 1.39$  Myr; Chmeleff et al., 2010; Korschinek et al., 2010) and  $^{26}\text{Al}$   
61 ( $t_{1/2} = 705$  kyr; Nishiizumi, 2004) in rock surfaces is governed by complex exposure, erosion, and ice burial  
62 histories (Gosse and Phillips, 2001; Fabel et al., 2002; Stroeven et al., 2002). When a surface is buried by  
63  $>30$  m of ice, production is reduced to  $<1\%$  of that at the surface, and radionuclides, if present, will decay  
64 at known rates to concentrations supported by production at those depths. It is not possible to resolve  
65 complex glacial histories of ice burial and exposure arising from late Pleistocene and Holocene glacier



66 fluctuations by pairing long-lived nuclides such as  $^{10}\text{Be}$  and  $^{26}\text{Al}$  since neither will decay significantly in  
67 that time frame. However, pairing a long-lived nuclide with short-lived *in situ* cosmogenic  $^{14}\text{C}$  (*in situ*  $^{14}\text{C}$ ,  
68  $t_{1/2} = 5.7$  kyr) enables such complex histories to be constrained. This has been demonstrated in the European  
69 Alps (Goehring et al., 2011; Wirsig et al., 2016; Schimmelpfennig et al., 2022), on Greenland and Baffin  
70 Island (Briner et al., 2014; Young et al., 2021), in Antarctica (Johnson et al., 2019; Nichols et al., 2019;  
71 Balco et al., 2023), and in Norway (Rand and Goehring, 2019).

72 Another common method to reconstruct past glacier extent and activity is to study proglacial lake sediment  
73 records (Karlén, 1988; Nesje et al., 2000; Rosqvist et al., 2004; Nielsen et al., 2016; Aa and Sønstegeard,  
74 2019; Røthe et al., 2019). Typically, glacial sediments in a lake record (glacial flour) indicate an active  
75 glacier within the lake catchment while a prevalence of organic-rich sediments (gyttja) indicates deposition  
76 during a period of glacial inactivity or absence (Jansson et al., 2005). This is because basal sliding by a  
77 warm-based glacier is required for a glacier to erode its substrate and produce glacial flour. However,  
78 several other factors influence the sedimentation rate in proglacial lakes, such as hydrological regime,  
79 intermediate sediment storage capacity, and the activity of other geomorphological processes within the  
80 catchment (Leonard, 1986; Rubensdotter and Rosqvist, 2003; Jansson et al., 2005). In a setting with a  
81 sequence of lakes acting as sediment traps, glacial lake sedimentation may constrain the ice extent  
82 (Jansson et al., 2005; Nesje, 2009).

83 Climate reconstructions based on vegetation development and lake sediment proxy records indicate that the  
84 climate in northern Sweden warmed rapidly and that conditions were relatively wet (Shemesh et al., 2001;  
85 Sjögren and Damm, 2019) when the Fennoscandian Ice Sheet (FIS) melted (Kullman and Öberg, 2015;  
86 Sjögren, 2021). Even warmer but also drier summer conditions characterize the so-called Holocene Thermal  
87 Maximum (HTM;  $\sim 8 - 5$  ka; Barnekow, 2000; Seppä et al., 2005; Sjögren, 2021; Wastegård, 2022). Based  
88 on sediment stratigraphies in proglacial lakes, Karlén (1976, 1981, 1988) proposed that some Swedish  
89 glaciers advanced during this time while others may have melted away, in line with records from some  
90 Norwegian glaciers (Bjune et al., 2005; Nesje et al., 2008; Nesje, 2009). Proglacial lake records show that  
91 glacier activity generally increased in response to an overall cooling trend after 5 ka, a progression that is  
92 documented across the Arctic (Karlén et al., 1995; Matthews and Dresser, 2008; Kaufman et al., 2009;  
93 Larocca and Axford, 2022). The latest period of glacier reactivation was during the Little Ice Age (1500-  
94 1900 CE), and evidence for this is rich compared to earlier periods (Grove, 2004; Matthews and Briffa,  
95 2005).

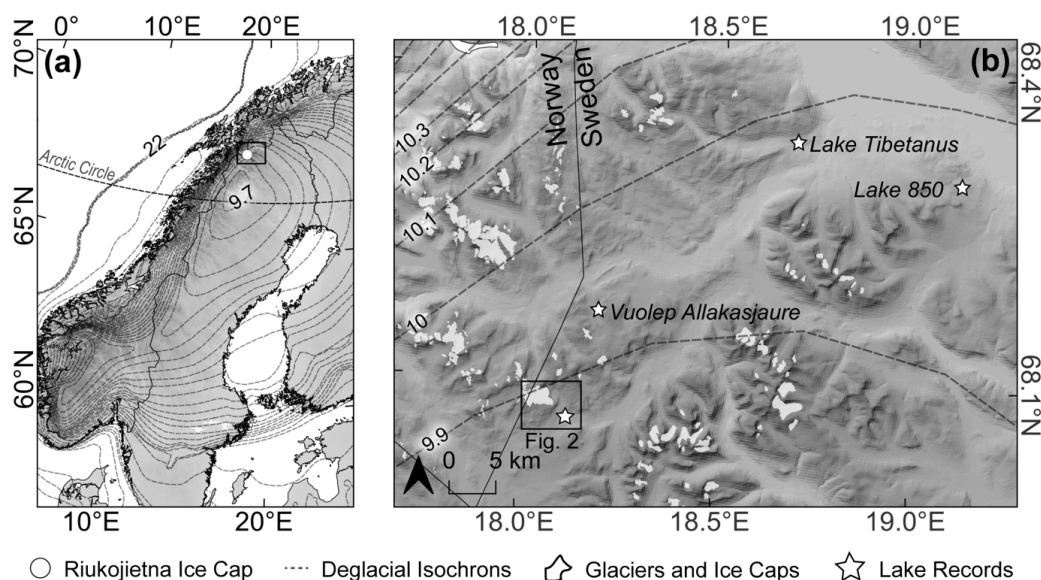
96 Based on lichenometric dating of end moraine ridges, Karlén (1988) inferred that most Swedish glaciers  
97 reached their maximum Holocene position sometime during the 18<sup>th</sup> century and, supported by the oldest  
98 photographic evidence (Svenonius, 1910), again as late as ca. 1910 CE. Geomorphic evidence of earlier



99 Holocene advances was potentially eradicated during this time (Jansson et al., 2005). Sediments from  
100 proglacial lakes therefore constitute the best continuous archive of Holocene glacier activity.

101 Here, we aim to constrain the former size and activity of Riukojietna (Sámi: Rivgojehkki), a rapidly  
102 retreating ice cap located in northern Sweden (Fig. 1). We do this by combining direct evidence for ice-free  
103 conditions and ice-burial durations from cosmogenic nuclide chronometry (*in situ*  $^{14}\text{C}$ ,  $^{10}\text{Be}$ ,  $^{26}\text{Al}$ ) and  
104 indirect evidence of glacial extent and activity derived from proglacial lacustrine records, complemented  
105 with ice-cap reconstructions based on historical records. This allows us to present the first full Holocene  
106 glacial history of a Swedish glacier based on multi-proxy records, and evaluate its sensitivity to Holocene  
107 climate change.

108  
109



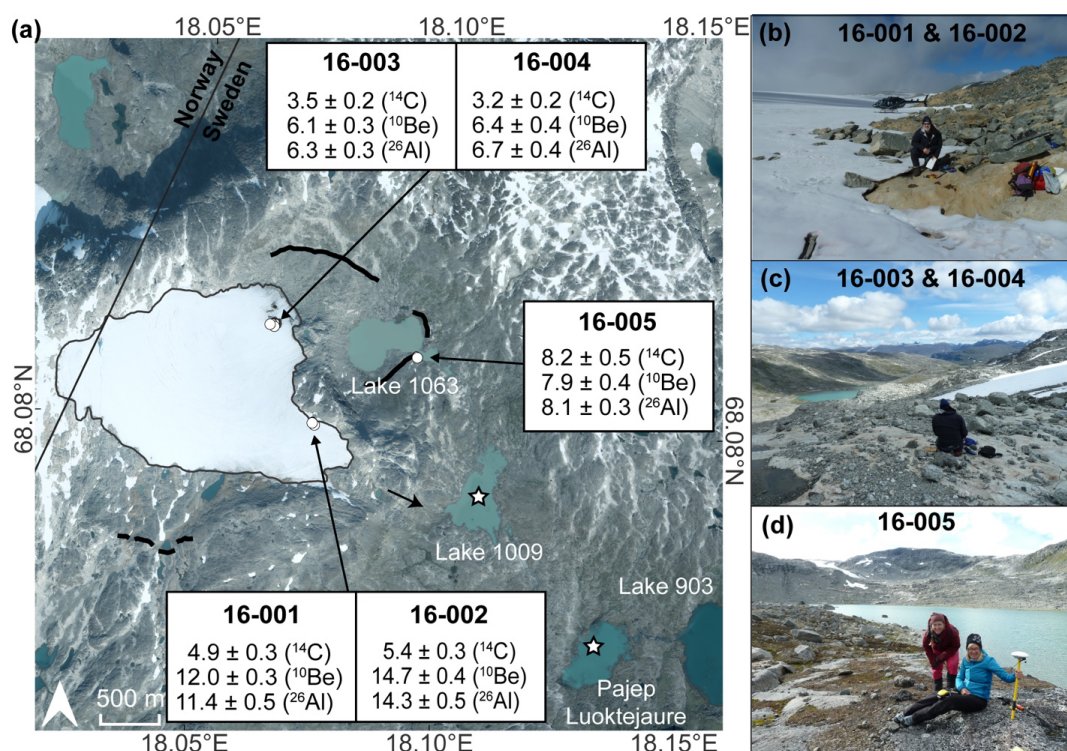
110 ○ Riukojietna Ice Cap    - - - Deglacial Isochrons    ⊕ Glaciers and Ice Caps    ☆ Lake Records  
111 **Figure 1:** (a) Map showing deglacial isochrons of the Fennoscandian Ice Sheet (Stroeven et al., 2016) in 100-year  
112 intervals around the location of Riukojietna (box with white dot: panel b). (b) European Union Digital Elevation  
113 Model (EU-DEM) of northern Sweden/Norway depicting the location of glaciers, including Riukojietna (box: Fig.  
114 2a). The numbers on the contours are deglacial isochrons in cal ka BP (Stroeven et al., 2016). Modified from  
115 Koester (2023).

## 116 2 Study site

117 Riukojietna is a small, thin (thickness <100 m), polythermal ice cap covering a plateau on the Swedish-  
118 Norwegian border (Fig. 2). This ice cap is ideal for studying Late Pleistocene to Holocene glacier  
119 fluctuations using cosmogenic nuclides and lake sediments for two reasons (Koester, 2023). First, the ice  
120 cap rests on quartz-rich bedrock of the Kõli Nappe which allows for the application of multiple nuclides,



121 including  $^{10}\text{Be}$ ,  $^{26}\text{Al}$ , and *in situ*  $^{14}\text{C}$ . In contrast, most glaciers in northern Sweden are situated in the  
 122 higher alpine areas where amphibolite and metadolerite bedrock of the Seve Nappe dominates  
 123 (Andréasson and Gee, 1989; Bergman et al., 2012). Second, a thin and blocky till cover, gentle slopes,  
 124 and an absence of sediment-rich landforms in the catchment implies that glacial flour is the dominant  
 125 source of minerogenic material in downstream lakes. As such, we expect lake records from the catchment  
 126 to primarily reflect fluctuations in glacier activity and extent.  
 127



128 **Figure 2:** (a) Google Earth satellite image (2018; Map data: Google, © 2025 CNES / Airbus) of the Riukojietna ice  
 129 cap depicting the location of bedrock samples (white circles). Simple exposure ages (in ka) are shown in white  
 130 boxes. Thick black lines depict the location of Late Holocene moraines. Black arrow indicates a possible earlier  
 131 extension direction of the ice cap. White stars depict lakes that have been cored downstream of the ice cap. (b) Two  
 132 bedrock samples collected directly adjacent to the ice cap (1290 m a.s.l.). (c) Two bedrock samples collected from a  
 133 bedrock knob that was exposed in 2011 (1240 m a.s.l.). (d) One bedrock sample collected adjacent to Lake 1063  
 134 outlet (1064 m a.s.l.). Modified from Koester (2023).  
 135  
 136

137 Riukojietna had an area of 5.5 km<sup>2</sup> and 4.6 km<sup>2</sup> when surveyed from 1960 and 1978 aerial photographs,  
 138 respectively (Rosqvist and Østrem, 1989; Table 1). However, the ice cap has continued to shrink,  
 139 covering a mere 2.8 km<sup>2</sup> and thinned to span only 283 m vertically between the ice divide and the snout in  
 140 2015 (Table 1). The ice cap flows radially outwards from its highest point and is impounded by bedrock



141 ridges to the south and northeast. Currently, Riukojietna has one outlet glacier tongue that terminates on a  
142 steep rise to the northeast (Fig. 2). The position of this tongue has been mapped since 1963 and the glacier  
143 mass balance has been monitored annually since 1986 revealing high sensitivity to changes in summer  
144 temperature and winter precipitation (WGMS, 2025). Two topographic maps were constructed based on  
145 aerial photography from 1960 and 1978 showing ice cap surface topography and extent (Rosqvist and  
146 Østrem, 1989). The eastern terminus calved into Lake 1063 (Fig. 2) before 1960 but retreated up-valley  
147 after 1975. Ice volume has been decreasing significantly during the 20<sup>th</sup> century (Table 1) due to a  
148 dominantly negative annual mass balance (WGMS, 2025). Because it is relatively low-elevation and  
149 spans an unusually narrow elevation interval compared to most valley glaciers in the region, Riukojietna  
150 is regarded to be highly sensitive to climate change (Rosqvist and Østrem, 1989; Koester, 2023).

151 Four lakes on the eastern side of the ice cap act as a series of traps for sediment derived from glacial  
152 erosion. Ordered by decreasing elevation (in m a.s.l.), they are lakes 1063, 1009, Pajep Luoktejaure (913;  
153 where “Pajep” means upper and “jaure” means lake– so Upper Luokte lake), and Vuolep Luoktejaure  
154 (903) (or Lower Luokte lake, which is only partially visible in Fig. 2). Lakes at this latitude and altitude  
155 are generally ice-covered from October to June (Rosqvist et al., 2004). From the variations in relative  
156 densities and organic content in sediment cores from Lake 1009 and Pajep Luoktejaure, Karlén (1981,  
157 1988) proposed that Riukojietna was inactive and small, or disappeared, between  $10.9 \pm 0.4$  (Si-2860) and  
158  $2.7 \pm 0.1$  (Si-2859) cal ka BP (re-calibrated bulk sediment samples using the online CALIB Radiocarbon  
159 Calibration v 8.2; Stuiver and Reimer, 1993; Reimer et al., 2020) and that the ice cap subsequently  
160 reactivated.

161 The relatively prominent lateral/end moraine sequence consisting of large boulders located to the  
162 northeast and east of Lake 1063 (Fig. 2) indicates that the ice cap advanced to this position at least once  
163 during the Holocene. A depositional age of c. 1910 CE was inferred for this ridge (Pohjola et al., 2005)  
164 based on lichenometry of *Rhizocarpon geographicum* and *Rhizocarpon alpicola* (Karlén, 1973), which is  
165 similar to other lichenometry-dated Little Ice Age (LIA) moraines in the region (Karlén, 1976; Karlén and  
166 Denton, 1976). A less prominent moraine ridge indicates that the glacier once extended down the  
167 southwestern slope of the plateau (Fig. 2). A glacially molded plateau surface extends from the current ice  
168 cap margin towards the southeast (arrow, Fig. 2), indicating a possible earlier extension direction of the  
169 ice cap towards Lake 1009 (Koester, 2023).

170

171

172



173  
174  
175

**Table 1:** *Riukojietna area, thickness, and volume reconstructions since the LIA (Wahlström, 2016).*

Year (CE)	1910	1960	1978	2015
Area (km <sup>2</sup> )	6.7	5.5	4.6	2.8
Volume (km <sup>3</sup> )	0.36	0.26	0.22	0.13
Min altitude (m a.s.l.)	1058	1058	1122	1146
Max altitude (m a.s.l.)	1488	1468	1459	1429
Elevation span (m)	430	410	337	283
Average thickness (m)	54	47	47	46
Volume decrease in % (from 1910 CE)	--	28	39	64

176

### 177 **3 Methods**

178 We combine cosmogenic nuclide chronometry, lacustrine sediment records, historic ice cap  
179 reconstructions, and modeling of complex exposure histories to evaluate the Holocene history of  
180 Riukojietna (Koester, 2023). Each method is described in detail below.

#### 181 **3.1 Cosmogenic nuclide sampling and analysis**

182 We collected five granitic bedrock samples with angle grinder, hammer, and chisel from three locations  
183 near Riukojietna in August 2016 and measured concentrations of *in situ* <sup>10</sup>Be, <sup>26</sup>Al, and <sup>14</sup>C (Fig. 2, Table  
184 2). Two samples were collected from the base of a small bedrock ridge immediately adjacent to the ice  
185 cap (<2 m from the modern ice; Riuko-16-001 and 16-002). Two samples were taken from a bedrock  
186 knob protruding through the outlet glacier tongue that became exposed in 2011 (Riuko-16-003 and 16-  
187 004). In the following, we collectively refer to these two sites as ‘ice-marginal bedrock’. The last sample  
188 was collected from a bedrock outcrop adjacent to the outlet of Lake 1063 (Riuko-16-005), in the  
189 following referred to as the ‘lake outlet sample’.

190 We separated quartz at the Purdue Rare Isotope Measurement Laboratory (PRIME Lab) using standard  
191 mineral separation procedures (<https://www.physics.purdue.edu/primelab/labs/mineral-separation-lab/procedure.php>). Samples were crushed, sieved to 250-500 μm, and magnetic minerals removed using  
192 a Carpco magnetic separator. Micas and feldspars were removed with froth flotation, and the remaining  
193 quartz separate was subsequently leached in weak hydrofluoric (HF) and nitric acids (HNO<sub>3</sub>) to remove  
194 meteoric <sup>10</sup>Be (Kohl and Nishiizumi, 1992). Quartz purity was assessed with inductively coupled plasma-  
195 optical emission spectrometry (ICP-OES) at PRIME Lab (Al target: <200 ppm). Riuko-16-002 and  
196 Riuko-16-005 had high Al and Na contents, indicating the presence of feldspars, and were therefore  
197 subjected to an additional separation step using heavy liquids and etching in weak acids. We have never  
198 observed any demonstrable effects from froth flotation on PRIME Lab *in situ* <sup>14</sup>C measurements using



200 these quartz purification procedures, thus no additional steps were taken (e.g., Nichols and Goehring,  
201 2019).

202 Beryllium and aluminum were extracted at PRIME Lab following the procedures outlined in Andersen et  
203 al. (2020). Beryllium samples were spiked with ~0.26 mg of Be carrier and aluminum samples were  
204 spiked with 0.9-1.3 mg of Al carrier if they didn't contain enough native Al before digestion in HF (target  
205 ~1.5 mg Al). The samples were prepared in one batch with a procedural blank and an aliquot of the  
206 intercomparison material CoQtz-N (Binnie et al., 2019). Be and Al were separated through anion and  
207 cation column chromatography, precipitated, oxidized, mixed with niobium powder, and pressed into  
208 cathodes for measurement. Isotopic ratios ( $^{10}\text{Be}/^9\text{Be}$  and  $^{26}\text{Al}/^{27}\text{Al}$ ) were measured by accelerator mass  
209 spectrometry (AMS) at PRIME Lab.  
210



**Table 2.** Sample information and measured cosmogenic nuclide concentrations.

Sample ID	Latitude ( $^{\circ}N$ )	Longitude ( $^{\circ}W$ )	Elevation (m a.s.l.)	Sample thickness (cm)	Density ( $g\ cm^{-3}$ )	Shielding	[ $^{10}Be$ ] ( $\times 10^5\ at\ g^{-1}$ )	[ $^{26}Al$ ] ( $\times 10^6\ at\ g^{-1}$ )	[ $^{14}C$ ] ( $\times 10^5\ at\ g^{-1}$ )
16-001	68.08005	18.07339	1291	1.5	2.65	0.99	$1.8107 \pm 0.0452$	$1.2158 \pm 0.0549$	$1.9242 \pm 0.0820$
16-002	68.08013	18.07315	1288	1.2	2.65	0.99	$2.2140 \pm 0.0534$	$1.5105 \pm 0.0538$	$2.0705 \pm 0.0856$
16-003	68.08749	18.06473	1238	1.5	2.65	0.99	$0.8825 \pm 0.0442$	$0.6391 \pm 0.0278$	$1.4580 \pm 0.0815$
16-004	68.08751	18.06409	1242	1.3	2.65	0.99	$0.9251 \pm 0.0590$	$0.6834 \pm 0.0431$	$1.3336 \pm 0.0800$
16-005	68.08550	18.09376	1064	1.4	2.65	1.00	$0.9918 \pm 0.0531$	$0.7170 \pm 0.0288$	$2.2698 \pm 0.0830$

210  
211

212



214 Carbon-14 was extracted at PRIME Lab using the automated Carbon Extraction and Graphitization  
215 System described by Lifton et al. (2023) and following procedures modified from that publication.  
216 Twenty grams of lithium metaborate ( $\text{LiBO}_2$ ) flux is first degassed for one hour at 1100 °C in a reusable  
217 Pt-Rh boat (90% Pt, 10% Rh) in ~ 6.67 kPa of Research Purity  $\text{O}_2$ , allowed to cool overnight under  
218 vacuum, and then approximately 5 g of sample quartz is evenly distributed over the solidified  $\text{LiBO}_2$ . The  
219 sample is then combusted at 500 °C for one hour in ~ 6.67 kPa of Research Purity  $\text{O}_2$  to remove  
220 atmospheric/organic contaminants, and the system is evacuated. Approximately 6.67 kPa of Research  
221 Purity  $\text{O}_2$  is then added to the system, and the sample is heated to 1100 °C for three hours to release any  
222 trapped carbon species. All evolved C species are oxidized to  $\text{CO}_2$  by passing the process gas over 2 mm  
223 quartz beads at ~ 950 °C. After extraction, the evolved gas is collected in a coil trap cooled with liquid  
224 nitrogen, purified using a variable temperature trap at -145 °C and passed over Cu mesh and Ag wool  
225 held at 600 °C to remove contaminants, before volume measurement and dilution with  $^{14}\text{C}$ -free  $\text{CO}_2$  to the  
226 equivalent of ~ 300  $\mu\text{g C}$ . Finally, a ca. 9  $\mu\text{g C}$  split is collected for stable C isotopic measurement, and  
227 the remaining sample is reduced to graphite in Research Purity  $\text{H}_2$  over an Fe catalyst before packing into  
228 a cathode for AMS measurement (e.g., Santos et al., 2004, 2007).

229 Sample  $^{14}\text{C}/^{13}\text{C}$  ratios were measured by AMS relative to Oxalic Acid II (NIST-4990C) at Purdue  
230 University. Stable carbon isotopic ratios were measured at the University of California Davis Stable  
231 Isotope Facility using isotope ratio mass spectrometry (e.g., Lifton et al., 2023). The  $^{14}\text{C}$  concentration is  
232 calculated from the measured  $^{14}\text{C}/\text{C}_{\text{total}}$  after subtracting out representative procedural background  $^{14}\text{C}$   
233 (Hippe and Lifton, 2014).

234 We use the primary CRONUS-Earth global calibration production rates for  $^{10}\text{Be}$  ( $3.9 \pm 0.3$  at  $\text{g}^{-1} \text{yr}^{-1}$ ),  $^{26}\text{Al}$   
235 ( $28.5 \pm 3.1$  at  $\text{g}^{-1} \text{yr}^{-1}$ ) and *in situ*  $^{14}\text{C}$  ( $12.8 \pm 0.9$  at  $\text{g}^{-1} \text{yr}^{-1}$ ) to calculate exposure ages and model ice burial  
236 and erosion histories (Lifton et al., 2014, 2016; Borchers et al., 2016; Phillips et al., 2016). The *in situ*  $^{14}\text{C}$   
237 production rate also includes the Young et al. (2014) *in situ*  $^{14}\text{C}$  calibration dataset (Koester and Lifton,  
238 2023, 2024). All calculations utilize nuclide-specific LSDn scaling (Lifton et al., 2014, 2016) and the  
239 muon production formulation from Balco (2017). Simple exposure ages (i.e., assuming continuous  
240 exposure with no erosion or burial) were calculated using the online University of Washington  
241 cosmogenic calculator, v.3 (wrapper script 3.0.2, constants: 2024-08-26, muons: 1A; Balco et al., 2008;  
242 <https://hess.ess.washington.edu/math/>), with *in situ*  $^{14}\text{C}$  production rates calibrated using the above  
243 datasets.



244 **3.2 Lacustrine sediment cores**

245 Pajep Luoktejaure has a relatively even bathymetry with one deeper section (12 m) in its northern part.  
246 We retrieved a deep core (1995) and five surface and deep cores (PL1 – PL5) from the deepest part of the  
247 lake in April 1995 and April 1998, respectively. We used a gravity corer to retrieve an undisturbed  
248 surface sample (top 25 cm; PL3) and a modified Livingstone piston corer (90 mm diameter) for the others  
249 (1995; PL1, 2, 4, and 5). Visual inspection and results from measurements of loss-on-ignition (LOI),  
250 determined at 550 °C with 1 cm resolution, for PL1 – PL4 show the same general stratigraphy for  
251 common sections (PL5 remains unopened, for reference). PL1-169 is the longest core (down to 169 cm  
252 below the lake floor) and the only one representing the early phase of lake development. The composite  
253 stratigraphic description of Pajep Luoktejaure is based on this core and surface core PL3-25.

254 Sedimentary structures and grayscale densities of cores PL1-169 and PL3-25 were determined by X-ray  
255 radiography (Rosqvist et al., 2004). Line transects (1 mm width) of grayscale density values were taken at  
256 a resolution of 0.3 mm. In this study, grayscale density is merely used to identify areas of lamination.  
257 Grain size distribution was analyzed in a SediGraph 5100 on 1 cm slices of specific sedimentary  
258 structures (*i.e.*, finely laminated minerogenic sections at 115-116 cm and 8-10 cm depths in core PL1-  
259 169).

260 Age control is provided by four samples from Pajep Luoktejaure; three AMS <sup>14</sup>C-dates from core PL1-  
261 169 and one from near-surface sediments in the core of 1995 (Table 3). We also used a basal date derived  
262 from a terrestrial plant macrofossil from nearby lake Vuolep Allakasjaure to help constrain the timing of  
263 deglaciation (Table 3). The samples were radiocarbon dated at the Ångström Laboratory, Uppsala  
264 University, and converted to calendar ages using the IntCal20 calibration curve (Reimer et al., 2020).  
265 Three of the radiocarbon constraints were used to derive an age–depth model using the Bayesian  
266 accumulation age-modelling software of Blaauw and Christen (2011; Fig. S1).

267  
268



269 **Table 3:** Radiocarbon chronology for Pajep Luoktejaure. Three radiocarbon dates were derived from core PL1-169  
 270 at 116 cm depth (1 cm bulk sample), 90 cm depth (terrestrial macrofossil), and 9 cm depth (1 cm bulk sample). The  
 271 latter replicated the date from a 12 cm depth terrestrial macrofossil sample of the same stratigraphic unit in the  
 272 1995 core from Pajep Luoktejaure. The basal bulk sediment age was replicated with a terrestrial macrofossil date  
 273 from the same stratigraphic position (first radiocarbon accumulation after deglaciation) from nearby lake Vuolep  
 274 Allakasjaure (12 km distance; Rosqvist et al., 2004; Fig. 1b). Calibrated ages derived using CALIB Radiocarbon  
 275 Calibration v 8.2 (<http://calib.org/calib/>; Stuiver and Reimer, 1993; Reimer et al., 2020).  
 276

Sample Name	Depth (cm)	Material	<sup>14</sup> C Age (yr BP)	δ <sup>13</sup> C (‰ VPDB*)	Calibrated Age (cal ka BP)
<i>Pajep Luoktejaure</i>					
Ua-14024	9	bulk sediment	1920 ± 70	-27.1	1.8 ± 0.1
Ua-14025	90	macrofossil	4024 ± 85	-27.5	4.5 ± 0.1
Ua-14026	116	bulk sediment	9650 ± 160	-26.9	11.0 ± 0.1
Ua-4751	12	macrofossil	1896 ± 70	-26.2	1.8 ± 0.1
<i>Vuolep Allakasjaure (Rosqvist et al., 2004)</i>					
Ua-16628	155	macrofossil	8740 ± 100	-23.0	9.8 ± 0.2

277 \* Measured relative to the Vienna Peedee Belemnite standard

278

### 279 3.3 Modern ice thickness reconstructions, bed topography, and volume calculations

280 Detailed ice surface topographic maps were constructed from aerial photographs taken in 1960 and 1978  
 281 to determine the average mass balance of Riukojietna (Rosqvist and Østrem, 1989). These two maps,  
 282 reproduced at 1:10 000 in the back sleeve of *Geogr. Ann.*, 71A (1-2), were scanned and georeferenced in  
 283 QGIS software to derive the ice-cap surface elevation during these years. The ice-cap topography was  
 284 additionally mapped during the summer of 2014 and spring of 2015 using two differential GPS (dGPS)  
 285 rover units. The subglacial bedrock topography was constrained with ground penetrating radar (GPR)  
 286 towed behind a snowmobile in the springs of 2011, 2012, and 2015 (Fig. S2). We use these data sources  
 287 to track ice cap area and volume changes relative to a 2-m-resolution LiDAR digital elevation model  
 288 (DEM) from 2015 (Fig. S2).

289 The elevations of fixed bedrock points on the 1960 and 1978 maps were compared to the recent LiDAR  
 290 DEM to evaluate their accuracies, and differences were calculated. These differences were interpolated  
 291 using kriging in Surfer 11 to create misfit values across the glacier surface. The resulting spatial pattern of  
 292 misfit is used to correct the altitudes derived from the 1960 and 1978 maps to better match ice surface  
 293 elevations to the 2015 LiDAR DEM (Fig. S3).

294 The perimeter of the presumed LIA glacial extent (1910 CE) was mapped from the 1960 and 1978  
 295 orthophotos and integrates the location of the eastern terminal moraine. As there are no moraines limiting  
 296 previous extents on the western side, we assumed a 50 – 100 m more expanded glacier relative to its



297 extent in 1960. The 1910 CE ice surface was calculated for the central flow line (Fig. S4) using the  
298 reconstructed bed topography, a target maximum elevation of 1490 m a.s.l. based on a summit ice  
299 thickness of c. 93 m estimated by Pohjola et al. (2005), and an adjustable yield stress following Benn and  
300 Hulton (2010). The surface elevations were interpolated in Surfer 11 using kriging to create an LIA ice  
301 surface reconstruction. For each of the four time slices, Surfer 11 was used to calculate the volume and  
302 average ice thickness of Riukojietna using the difference between the ice surface DEM and the bed  
303 topography DEM (Table 1).

### 304 3.4 Modeling complex exposure histories

305 We explore potential effects of temporal variations in ice cap thickness on our ice-marginal bedrock  
306 cosmogenic nuclide inventories (Riuko-16-001 to 16-004) using a Lagrangian forward modeling  
307 framework (e.g., Knudsen et al., 2019) implemented in MATLAB (code reference – to be added before  
308 publication). This model predicts the post-LGM time evolution of  $^{10}\text{Be}$ ,  $^{26}\text{Al}$ , and  $^{14}\text{C}$  concentrations in  
309 bedrock during subaerial exposure and when either completely (ice > 30 m thick) or incompletely  
310 shielded beneath thin ice (< 30 m thick) from both spallogenic and muogenic production, while allowing  
311 for subglacial erosion. Modeling details are provided in the Supplement.

## 312 4 Results

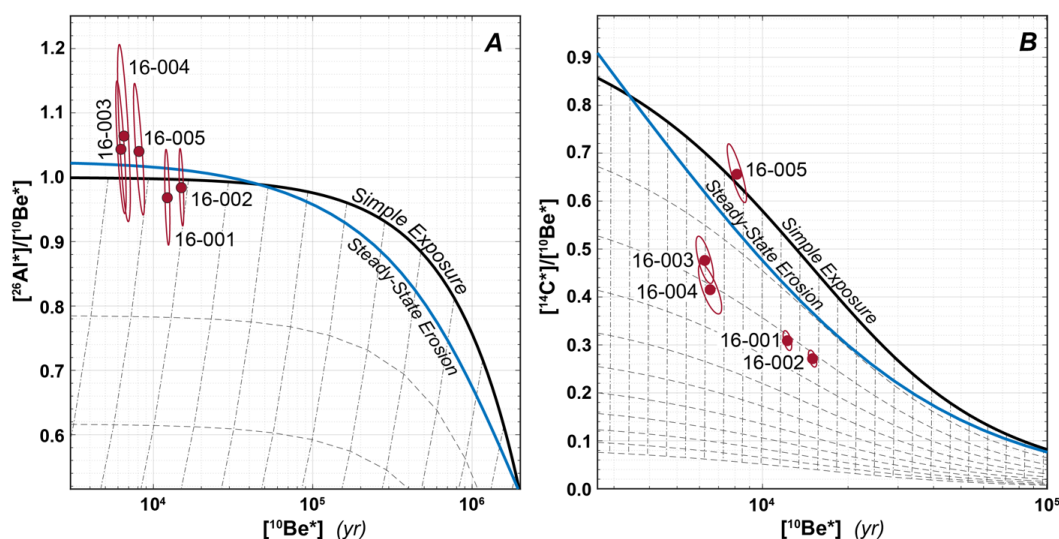
### 313 4.1 Cosmogenic nuclide concentrations and simple exposure ages

314 The  $^{10}\text{Be}$  concentrations in bedrock samples Riuko-16-001 to 16-005 range from  $8.8 \pm 0.4 \times 10^4$  to  $2.2 \pm$   
315  $0.1 \times 10^5$  atoms  $\text{g}^{-1}$ , while the  $^{26}\text{Al}$  concentrations range from  $6.4 \pm 0.3 \times 10^5$  to  $1.5 \pm 0.1 \times 10^6$  atoms  $\text{g}^{-1}$   
316 (Tables 2, S1; Koester, 2023). Measured *in situ*  $^{14}\text{C}$  concentrations range from  $1.3 \pm 0.1 \times 10^5$  to  $2.3 \pm 0.1$   
317  $\times 10^5$  atoms  $\text{g}^{-1}$  (Tables 2, S2; Koester, 2023). The corresponding simple exposure ages range between  $3.2$   
318  $\pm 0.2$  ka for *in situ*  $^{14}\text{C}$  and  $14.7 \pm 0.4$  ka for  $^{10}\text{Be}$  (Fig. 2; Tables S1 and S2). When plotted on a two-  
319 isotope diagram, the  $^{10}\text{Be}$ - $^{26}\text{Al}$  results of all five bedrock samples overlap with the simple exposure line at  
320  $1\sigma$  (Fig. 3a). In contrast, the  $^{14}\text{C}$ - $^{10}\text{Be}$  two-isotope diagram shows that only sample Riuko-16-005 overlaps  
321 the simple exposure line, indicating continuous exposure since deglaciation for that sample (Fig. 3b). All  
322 simple exposure ages for this sample agree within  $1\sigma$  (Fig. 2). We thus take the weighted mean  $^{14}\text{C}$ - $^{10}\text{Be}$ -  
323  $^{26}\text{Al}$  exposure age of  $8.1 \pm 0.1$  ka ( $1\sigma$ ) as the deglacial age for that location (Koester, 2023).

324 The remaining samples (Riuko-16-001 to 16-004) plot in the complex exposure field of the  $^{14}\text{C}$ - $^{10}\text{Be}$  two-  
325 isotope diagram (Fig. 3b). Because simple  $^{10}\text{Be}$  and  $^{26}\text{Al}$  exposure ages for the same samples overlap  
326 within  $1\sigma$ , we focus dominantly on the  $^{10}\text{Be}$  and  $^{14}\text{C}$  values in the remainder of the paper. The highest  
327 elevation site, adjacent to the current ice cap margin (~1290 m a.s.l.; Riuko-16-001 and 16-002), has the



328 oldest simple  $^{10}\text{Be}$  ( $^{14}\text{C}$ ) exposure ages of  $12.0 \pm 0.3$  ( $4.9 \pm 0.3$ ) and  $14.7 \pm 0.4$  ( $5.4 \pm 0.3$ ) ka, respectively  
 329 (Fig. 2). The two samples collected on the recently emerged bedrock knob at  $\sim 1240$  m a.s.l. (Riuko-16-  
 330 003 and 16-004) have younger  $^{10}\text{Be}$  ( $^{14}\text{C}$ ) simple exposure ages of  $6.1 \pm 0.3$  ( $3.5 \pm 0.2$ ) and  $6.4 \pm 0.4$  ( $3.2$   
 331  $\pm 0.2$ ) ka, respectively – internally consistent for each nuclide but disagreeing between nuclides (Koester,  
 332 2023).



333  
 334 **Figure 3:** (A) Two-isotope diagram of normalized  $^{26}\text{Al}/^{10}\text{Be}$  concentration ratio vs. normalized  $^{10}\text{Be}$  concentration.  
 335 Ellipses show  $2\sigma$  uncertainty. Normalization (indicated by \*) is to site production rates, hence the unit of  $[^{10}\text{Be}^*]$  is  
 336 yr. (B) Two-isotope diagram of normalized in situ  $^{14}\text{C}/^{10}\text{Be}$  concentration ratio vs. normalized  $^{10}\text{Be}$  concentration.  
 337 Burial isochrons (dashed lines) are calculated relative to the simple exposure curve. Burial isochron spacing is 500  
 338 kyr in A), and 2 kyr in B). Near-vertical dot-dashed lines are decay trajectories followed during burial. Asterisks  
 339 indicate that concentrations are normalized to site-specific production rates, hence corresponding units are in  
 340 years.

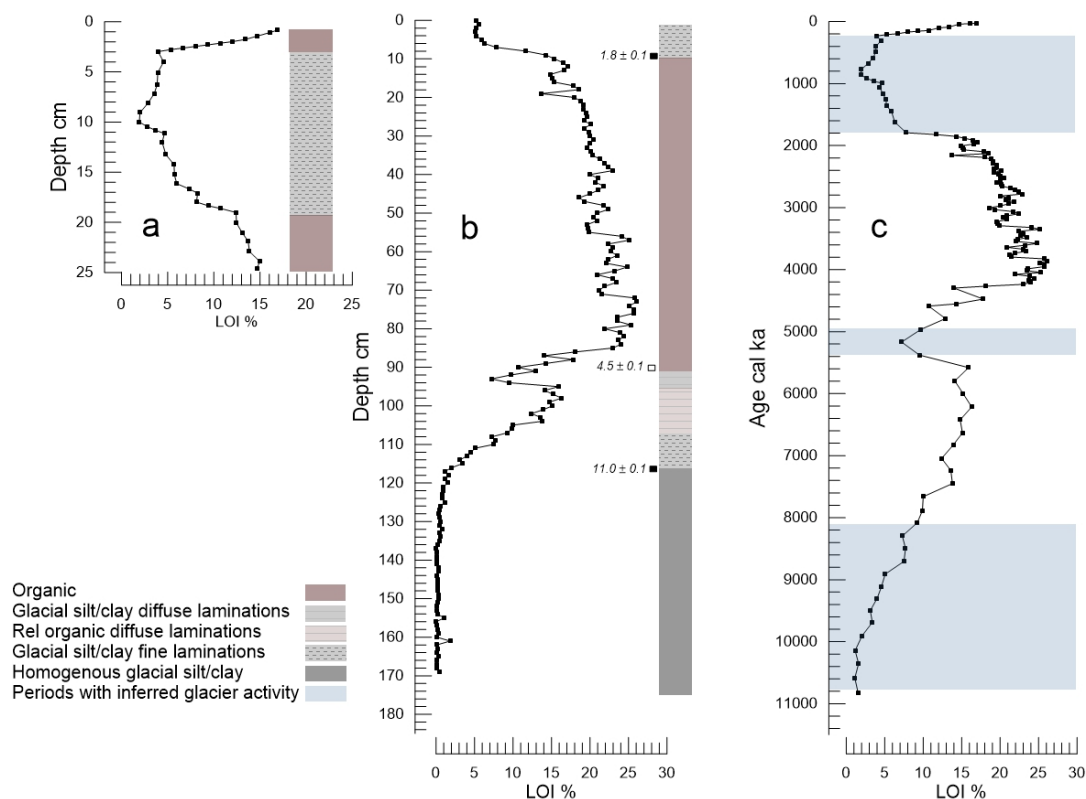
341

#### 342 4.2 Lacustrine records

343 The bottom of core PL1-169 from 169 to 116 cm depth is characterized by homogenous glacial silt and  
 344 clay (Fig. 4b) with LOI less than 2%. Between 116 and 107 cm depth, sediments are finely laminated silt  
 345 and clay with LOI less than 10%. Laminations become more diffuse between 107 and 95 cm depth and  
 346 LOI values increase, reaching as high as 16% at 98 cm depth. A drop in LOI to 7% at 93 cm is caused by  
 347 an influx of minerogenic matter. Homogenous gyttja with up to 26% LOI characterizes the sediments  
 348 between 90 and 10 cm depth. The uppermost 10 cm of PL1-169 consist of finely laminated silt and clay  
 349 with high density and low LOI (between 5% and 8%). Results from grain size distribution analyses show  
 350 indeed that the sampled sections consist of silt and minor amounts of clay (>90% silt/clay; i.e. <63  $\mu\text{m}$ ).



351 Surface core PL3-25 records the intact uppermost 25 cm of the stratigraphy in Pajep Luoktejaure (Fig.  
352 4a). Its sedimentary structure is similar to PL1-169 in the overlapping interval. Well-preserved  
353 laminations are observed between 19 and 3 cm. The topmost 3 cm of the core displays high LOI (up to  
354 17% at the surface). No laminations are detectable in these non-compacted organic surface sediments.  
355



356 **Figure 4:** Stratigraphy and loss on ignition (LOI %) from (a) surface gravity core PL3-25 and (b) Livingstone  
357 piston core PL1-169 in Pajep Luoktejaure (Fig. 2a). High LOI indicates high organic content, interpreted as  
358 relatively low glacial activity, while low LOI indicates low organic content associated with a relatively active  
359 glacier and minerogenic influx. Core PL1-169 has 3 radiocarbon tie points (in cal ka BP; Table 3). (c) Composite  
360 core LOI record against age, where 1 – 13 cm are from PL3-25 and 13 – 130 cm are from PL1-169. Age vs. depth  
361 for PL1-169 below 130 cm is poorly constrained. (Fig. S1).  
362

363 Three radiocarbon dates were obtained from PL1-169, with the oldest (116 cm depth;  $11.0 \pm 0.1$  cal ka  
364 BP; 2% LOI) and youngest (9 cm depth;  $1.8 \pm 0.1$  cal ka BP; 14% LOI) ages derived from bulk sediment  
365 and the intermediate age (90 cm depth;  $4.5 \pm 0.1$  cal ka BP) derived from a terrestrial plant macrofossil  
366 (Table 3). An additional radiocarbon date of a terrestrial macrofossil at 12 cm depth in the 1995 core, also  
367 representing the first deposition of late Holocene laminations in the core, replicates the bulk sediment age  
368 at 9 cm depth of  $1.8 \pm 0.1$  cal ka BP (Table 3). The basal radiocarbon age, from bulk sediment with only  
369 2% organic content, is much older than the expected regional  $\sim 9.8$  cal ka BP deglaciation age (Fig. 1b) of



370 Stroeven et al. (2016). Therefore, we adopt the basal sediment age from nearby lake Vuolep Allakasjaure  
371 (Fig. 1b; ~12 km NE of Pajep Luoktejaure) of  $9.8 \pm 0.2$  cal ka BP derived from a terrestrial macrofossil in  
372 the same stratigraphic position, that is, representing the first radiocarbon accumulation after deglaciation  
373 (Table 3; Rosqvist et al., 2004). Together with the two youngest radiocarbon ages (at 90 and 9 cm depth)  
374 and a sediment surface age of -48 BP (i.e., 1998 CE) they create the four tie points constraining the age-  
375 depth model (Fig. S1). To provide a composite record we spliced the core PL3-25 LOI record  
376 representing the top 13 cm of the sediment record into the PL1-169 LOI record (Fig. 4c). The average  
377 sedimentation rate of the upper laminated section is  $\sim 0.1$  mm year<sup>-1</sup> if the uppermost 3 cm corresponds to  
378 the time since the glacier retreated from the moraine at Lake 1063 at the end of the LIA. The  
379 sedimentation rate of the organic section (90 – 9 cm) is  $\sim 0.3$  mm year<sup>-1</sup>.

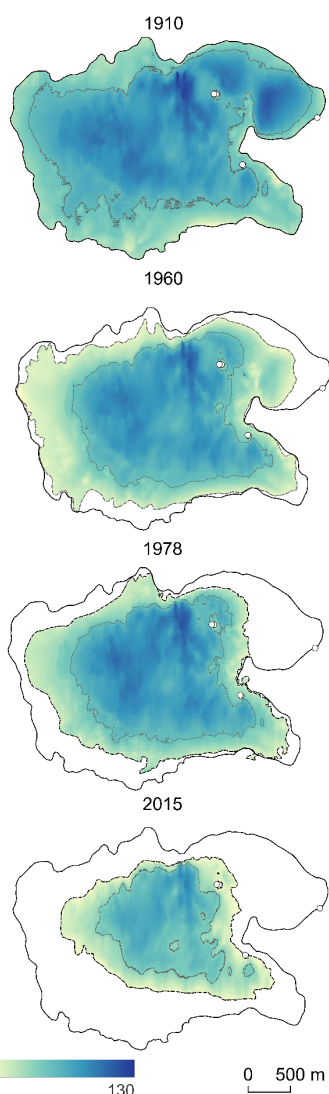
#### 380 **4.3 Ice thickness and volume reconstructions**

381 Ice thickness reconstructions for the past century are shown in Fig. 5. At the end of the LIA, Riukojietna  
382 covered an area of 6.7 km<sup>2</sup> and had an estimated volume of 0.36 km<sup>3</sup> (Table 1). Ice extent and volume  
383 have decreased by >58% and >64%, respectively, between 1910 CE and 2015 (Table 1; Fig. 5). Based on  
384 these reconstructions, we estimate that the ice thickness above our two ice-marginal cosmogenic sample  
385 locations (Riuko-16-001 to 16-004) started at 33-35 m one century prior to exposure (Table S4; Koester,  
386 2023).

### 387 **5 Discussion**

#### 388 **5.1 Constraints on the Holocene history of Riukojietna from cosmogenic nuclides**

389 The cosmogenic nuclide results offer constraints on the dimensions, including the minimum thickness of  
390 Riukojietna, through the Holocene (Koester, 2023). The agreement between <sup>14</sup>C-<sup>10</sup>Be-<sup>26</sup>Al simple  
391 exposure ages at 1σ for the lake outlet sample (Riuko-16-005; 1064 m a.s.l.) indicates continuous  
392 exposure at that site since deglaciation following erosional resetting of the surface. Thus, in relation to  
393 variations in minerogenic input seen in the lake record of Pajep Luoktejaure, this result establishes that  
394 Riukojietna did not cover or expand beyond the Lake 1063 outlet sampling site after  $8.1 \pm 0.1$  ka (mean  
395 of all three nuclide ages; Fig. 2). The result also reveals that the FIS, or Riukojietna, eroded sufficient  
396 bedrock at that site to remove any cosmogenic nuclide inventory produced prior to the Last Glacial  
397 Maximum (LGM).



398  
399  
400  
401  
402

**Figure 5:** Ice thickness reconstructions for Riukojietna from 1910 CE, 1960, 1978, and 2015 with respect to the maximum extent of 1910 CE (LIA extent). The 40 m ice thickness contour is shown in dashed grey. Sample sites are shown as white dots. Figure from Wahlström (2016).

403 The two samples from the highest altitude site (Riuko-16-001 and 16-002) from the bedrock ridge  
404 adjacent to the ice cap margin plot significantly below the continuous exposure field in the  $^{10}\text{Be}$ - $^{14}\text{C}$  two-  
405 isotope plot (Fig. 3b), indicating a complex exposure history. If one assumes glacial erosion to have  
406 completely removed any inherited component from exposure prior to the LGM, their position on this plot  
407 is consistent with a cumulative burial duration of 4 – 5 kyr. However, this simplest interpretation is



408 untenable because their simple  $^{10}\text{Be}$  exposure ages (of 12-15 ka) are older than the regional deglaciation  
409 age of ~9.8 ka (Stroeven et al., 2016; Fig. 2, Table 3), requiring additional contributions to  $^{10}\text{Be}$  inventory  
410 from pre-LGM exposure. Therefore, their position on the  $^{10}\text{Be}$ - $^{14}\text{C}$  two-isotope plot is skewed by inherited  
411  $^{10}\text{Be}$  and inferred burial durations are, therefore, difficult to quantify but likely shorter.

412 Like the highest-altitude samples, the samples from the bedrock knob (Riuko-16-003 and 16-004) also  
413 plot in the complex exposure field of the  $^{10}\text{Be}$ - $^{14}\text{C}$  two-isotope plot (Fig. 3b), consistent with 4 – 5 kyr of  
414 burial in the simplest interpretation of continuous exposure followed by burial and exposure by recent ice  
415 retreat. However, it is important to note that their position is also consistent with continuous postglacial  
416 exposure and an inherited  $^{10}\text{Be}$  component (smaller than that of Riuko-16-001 and 16-002) that would  
417 displace the position below the simple exposure curve.

## 418 **5.2 Constraints on the Holocene history of Riukojietna from lacustrine sediments**

419 Pajep Luoktejaure receives meltwater coming from the northeastern active outlet of Riukojietna (Fig. 2).  
420 Lakes 1063 and 1009 in its drainage system act as sediment traps. This will have a damping effect on  
421 sedimentary responses in Pajep Luoktejaure to changes in the activity and extent of Riukojietna.

422 Meltwater from the southeastern tongue of Riukojietna also enters Lake 1009 before it reaches Pajep  
423 Luoktejaure (Fig. 2). However, based on thermistor measurements in 1986 (Pohjola et al., 2005), the ice  
424 cap dome, and by inference its thin low-gradient southeastern tongue, were shown to be cold-based,  
425 which means that sub-glacial erosion is an unimportant component to downstream sediment delivery from  
426 that location during such restricted ice configurations. Although the Pajep Luoktejaure record may reflect  
427 some sediment contribution from this tongue during extended ice cap configurations (e.g., LIA), we  
428 estimate that its contribution is minor based on the topographic configuration (faint valley development  
429 and steep slope towards Lake 1009) implying that the ice would remain thin even in a more advanced  
430 position.

431 The basal section of homogenous glacial silt and clay in Pajep Luoktejaure (169-116 cm depth; Fig. 4b)  
432 represents an ice-dammed lake sequence. We suggest that this lake was formed by the retreating FIS  
433 margin obstructing water flow out of the valley, similar to the many ephemeral ice-dammed lakes that it  
434 dammed immediately to the north and east of Riukojietna (Ploeg and Stroeven, 2025). The subsequent  
435 laminated sediments that began accumulating from ca.  $9.8 \pm 0.2$  cal ka BP, with increasing LOI, indicate  
436 that organic production and seasonal input of meltwater from Riukojietna dominated the depositional  
437 signal after the northern FIS margin retreated from the site (Fig. 1b; Stroeven et al., 2016). The ice cap  
438 continued to deliver sediments to Pajep Luoktejaure after 9.8 ka, forming the 9 cm-thick laminated  
439 section, indicating that the glacier remained in a relatively advanced position during the early Holocene.



440 The following section with higher organic content and diffuse laminations between 107 and 91 cm depth  
441 (Fig. 4b), represents a time interval when the ice cap probably retreated sufficiently to also expose the  
442 Lake 1063 sediment trap. Our cosmogenic nuclide results indicate that Riukojietna covered Lake 1063  
443 until  $8.1 \pm 0.1$  ka, which we adopt as the constraining age for the start of this section. The increase in  
444 glacial sediment input and lowering of LOI between 94 and 92 cm depth indicates that Riukojietna  
445 delivered more sediment to downstream lakes, signaling a higher activity between 5.4 and 5.0 cal ka BP  
446 (Fig. 4b, c).

447 Subsequently, laminations disappear altogether and organic productivity increases to maximum Holocene  
448 levels. Possible paleoglaciological interpretations of this sedimentary section include that Riukojietna  
449 retreated and thinned to a configuration where it was as small or smaller than today with cold-based  
450 conditions inhibiting sub-glacial erosion, or that the ice cap melted away completely. Finely laminated  
451 glacial sediments in the top sections of PL1-169 and PL3-25 indicate a reactivation and expansion of  
452 Riukojietna starting shortly after  $1.8 \pm 0.1$  cal ka BP and culminating in 1910 CE. Finally, the decrease in  
453 glacial input and deposition of organic sediments in the topmost 3 cm reflects the time since  
454 Riukojietna retreated from its LIA and post-glacial maximum position marked by the moraine ridge  
455 fringing Lake 1063.

456 In summary, we infer that Riukojietna existed as an ice cap, and was more active and extensive than  
457 today, between 9.8 cal ka BP and 8.1 ka, during a short interval just before 5.0 cal ka BP, and between 1.8  
458 cal ka BP and 1910 CE. While these periods will determine the durations of sample burial in cosmogenic  
459 nuclide forward modeling in the next section, we acknowledge that the duration of burial during the mid  
460 Holocene, which is solely constrained by the lacustrine sediment record and radiocarbon dating, has the  
461 largest uncertainty due to a poor control on sediment accumulation rates.

### 462 **5.3 Constraints on Holocene history of Riukojietna from cosmogenic nuclide modeling**

463 While the lake sediments represent an indirect measure of the extent and state of Riukojietna, cosmogenic  
464 nuclide inventories in bedrock surfaces directly reflect the extent and state of Riukojietna through ice  
465 burial durations and erosion histories at the sampled sites. Here we test the ice history derived from the  
466 proglacial lake record by calculating the resulting cosmogenic nuclide concentration in ice-marginal  
467 bedrock sites arising from exposure and burial after FIS retreat.

468 Our reconstructed ice history for the ice-marginal bedrock sites (Riuko-16-001 to 16-004) relies on a set  
469 of assumptions based on derived cosmogenic nuclide concentrations, the composite lacustrine record, and  
470 a LIA ice-thickness reconstruction. First, we prescribe zero initial cosmogenic nuclide concentrations  
471 consistent with a complete removal of pre-LGM inventories and a thick (>50 m) ice cover until regional



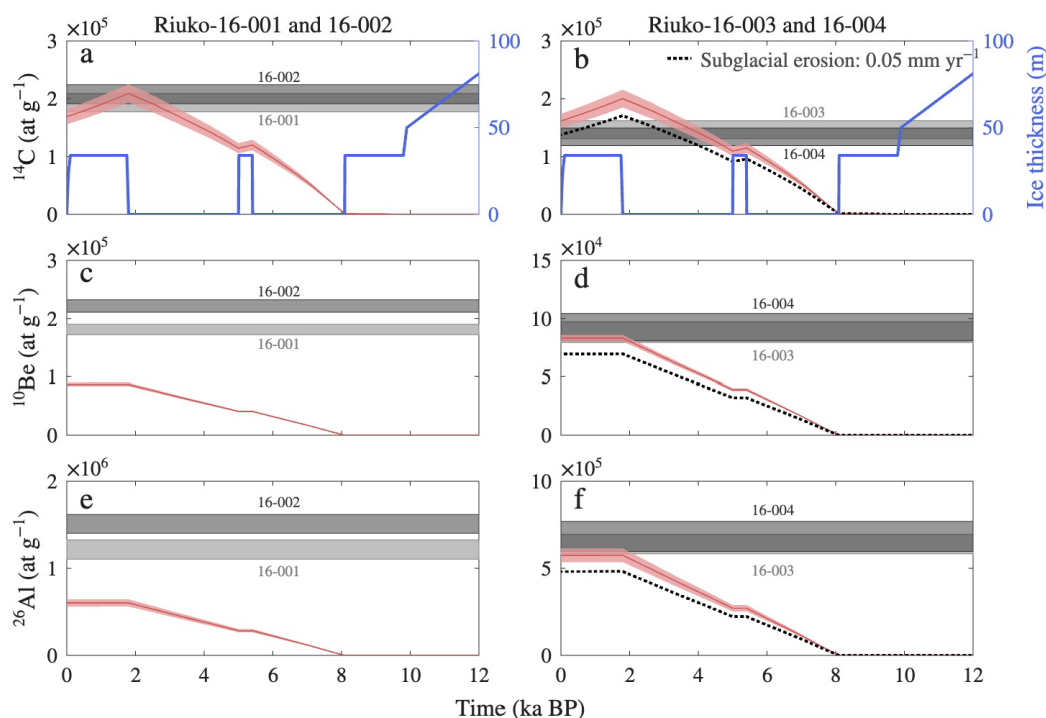
472 deglaciation at 9.8 cal ka BP (Stroeven et al., 2016). Second, we infer that Riukojietna extended over  
473 Lake 1063 until  $8.1 \pm 0.1$  ka as evidenced by the  $^{10}\text{Be}$ - $^{26}\text{Al}$ - $^{14}\text{C}$  weighted mean exposure age from sample  
474 Riuko-16-005. We therefore assume an ice thickness corresponding to the reconstructed LIA ice thickness  
475 over our samples (33-35 m; Fig. S4) between 9.8 cal ka BP and 8.1 ka. Third, the lake record shows  
476 evidence for a short mid-Holocene glacial advance between  $\sim 5.4$  and 5.0 cal ka BP, based on our age-  
477 depth model (Figs. 4c, S1). We therefore allow for complete sample site exposure from 8.1 ka to 5.4 cal  
478 ka BP followed by ice burial to 5.0 cal ka BP. Finally, our lake record indicates a re-advance after 1.8 cal  
479 ka BP. We therefore model full exposure from 5.0-1.8 cal ka BP, followed by ice burial until 1910 CE  
480 and ice thinning since, per our ice surface reconstructions (Section 4.3; Tables 1, S4; Figs. 5, 6, S4).  
481 However, uncertainties in the age-depth model are large (Fig. S1), and the median value we use might not  
482 capture shorter-term fluctuations in sedimentation rate. We thus also consider an alternate scenario  
483 without that mid-Holocene advance over our ice-marginal sites (Fig. 7).

484 The modeled *in situ*  $^{14}\text{C}$  inventories for Riuko-16-001 and 16-002 (without erosion) slightly  
485 underestimate the corresponding measured concentrations (slight overlap at  $2\sigma$  with Riuko-16-001, no  
486 overlap with Riuko-16-002; Fig. 6a), indicating slightly longer Holocene or late deglacial exposure  
487 duration than was modeled ( $\sim 400$  years). In contrast, the modeled  $^{10}\text{Be}$  and  $^{26}\text{Al}$  concentrations for those  
488 samples significantly underestimate the measured  $^{10}\text{Be}$  and  $^{26}\text{Al}$  concentrations, indicating a significant  
489 component of  $^{10}\text{Be}$  and  $^{26}\text{Al}$  derived from exposure prior to the LGM (Fig. 6c, 6e). Given its relatively  
490 rapid decay, we consider it highly unlikely that discrepancies between measured and modeled *in situ*  $^{14}\text{C}$   
491 can be explained through inheritance. Including erosion in the model for these samples would result in a  
492 worse fit between measured and modeled concentrations. The position of these samples, at a distance  
493 from faster flowing outlets, likely implies that they experienced cold-based, non-erosive ice conditions  
494 during the Holocene.

495 The modeled *in situ*  $^{14}\text{C}$  concentrations of Riuko-16-003 and 16-004 without erosion slightly overestimate  
496 the measured values but agree within  $2\sigma$  (Fig. 6b). As such, the *in situ*  $^{14}\text{C}$  inventories measured at this  
497 bedrock knob site are largely compatible with the history of Riukojietna inferred from downstream Pajep  
498 Luoktejaure and our Holocene ice shielding assumptions for that location. However, the modeled  $^{10}\text{Be}$   
499 and  $^{26}\text{Al}$  results for Riuko-16-003 and 16-004 without erosion slightly underestimate the corresponding  
500 measured concentrations (although agree within  $2\sigma$ ), indicating slightly longer exposure durations than  
501 was modeled (Fig. 6d, 6f). The position of Riuko-16-003 and 16-004 on an abundantly-striated bedrock  
502 knob emerging from an outlet glacier (Fig. S5), renders it worthwhile to model the potential effects of  
503 Holocene erosion on resulting concentrations. Including a subglacial erosion component of  $0.05 \text{ mm yr}^{-1}$   
504 during Holocene ice burial periods yields improved agreement with measured *in situ*  $^{14}\text{C}$  values over the



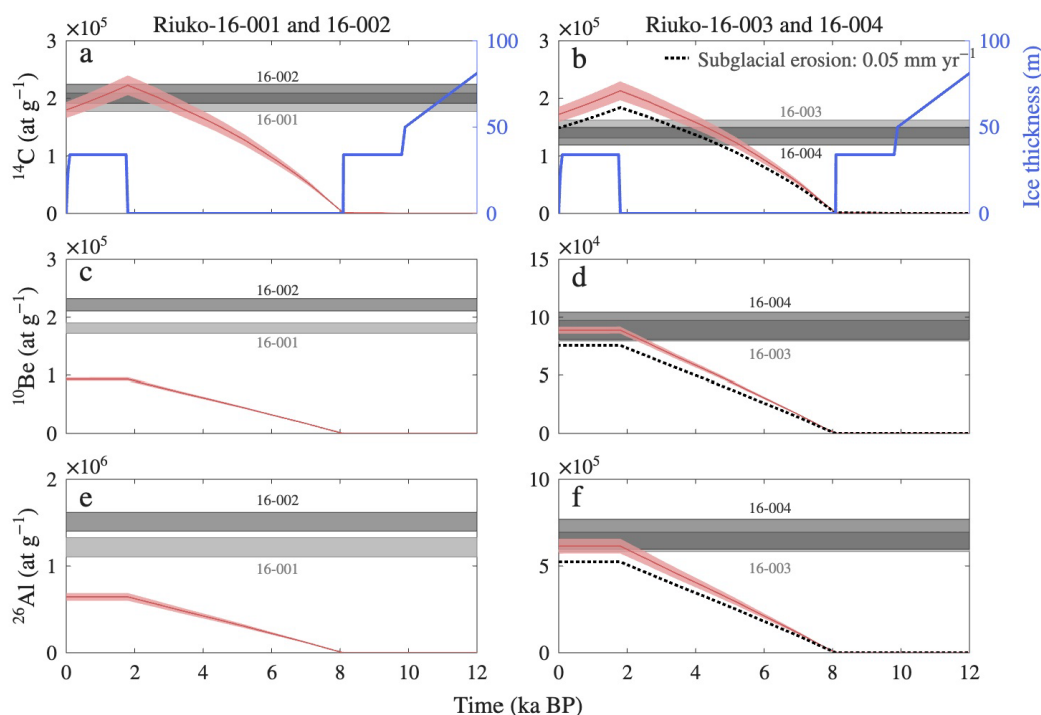
505 no-erosion scenario (Fig. 6b; black stippled line). However, including erosion worsens the fit with  
 506 measured values for  $^{10}\text{Be}$  and  $^{26}\text{Al}$  (Fig. 6d, 6f). A 400 year-longer Holocene exposure duration than  
 507 suggested by this reconstruction leads to an even better fit with the *in situ*  $^{14}\text{C}$  results at both sites when  
 508 simultaneously allowing for  $0.05 \text{ mm yr}^{-1}$  of subglacial erosion of the bedrock knob in the northeastern  
 509 outlet glacier (Fig. 7a and b). A component of inheritance is required to explain observed  $^{10}\text{Be}$  and  $^{26}\text{Al}$   
 510 nuclide concentrations in all ice-marginal samples (Figs. 6c-f, 7c-f). In summary, the ice-cap history  
 511 reconstructed from the lacustrine record, the lake-outlet cosmogenic sample, and the LIA ice thickness  
 512 reconstruction for Riukojietna, largely fits the measured *in situ*  $^{14}\text{C}$  concentrations in the two ice-marginal  
 513 bedrock sites.



514  
 515  
 516 **Figure 6:** Modeled cosmogenic nuclide accumulation (red) as a function of ice thickness (blue) based on the model  
 517 described in the text. The width of the red shading surrounding the modeled accumulation trace reflects the  
 518 cumulative effect of the production rate uncertainty in the sample. Panels a, c, and e show the results for samples  
 519 Riuko-16-001 and Riuko-16-002, while b, d, and f show results for samples Riuko-16-003 and Riuko-16-004 for  
 520 cases without subglacial erosion and with  $0.05 \text{ mm yr}^{-1}$  of subglacial erosion (dotted lines). Measured values of  
 521 each nuclide ( $\pm 2\sigma$  uncertainty) are indicated by gray shaded bands. Note that we track the cosmogenic nuclide  
 522 concentrations in the sample as it is exhumed to the surface (a Lagrangian approach) as opposed to tracking the  
 523 concentrations in the bedrock surface as rock is advected toward the surface by erosion (a Eulerian approach).  
 524



525 A rate of  $0.05 \text{ mm yr}^{-1}$  appears highly modest in a Swedish context where valley glaciers may have eroded  
526 their bedrock at ten times that rate (e.g., Schneider and Bronge, 1996). Having a difference in erosion  
527 between the two sites studied (Figs. 6, 7) is reasonable considering that basal sliding, and thereby glacial  
528 erosion, is likely higher at the bedrock knob site in the middle of the northeastern outlet glacier (where  
529 striations were abundant) than at the higher-elevation site flanking the southeastern and rather inactive  
530 tongue (where striations were absent). Encouragingly, a lower degree of inheritance is evident in the  
531 outlet glacier bedrock knob samples, aligning with inferred low rates of subglacial erosion for that site.  
532



533 **Figure 7:** Modeled cosmogenic nuclide accumulation (red) as a function of ice thickness (blue) based on the model  
534 described in the text – in this case with no mid-Holocene readvance modeled. The width of the red shading  
535 surrounding the modeled accumulation trace reflects the cumulative effect of the production rate uncertainty in the  
536 sample. Panels a, c, and e show the results for samples Riuko-16-001 and Riuko-16-002, while b, d, and f show  
537 results for samples Riuko-16-003 and Riuko-16-004 for cases without subglacial erosion and with  $0.05 \text{ mm yr}^{-1}$  of  
538 subglacial erosion (dotted lines). Measured values of each nuclide are indicated by gray shaded bands ( $\pm 2\sigma$   
539 uncertainty).  
540  
541

#### 542 5.4 Paleoclimate constraints

543 From our cosmogenic nuclide results and lake sediment record, we infer that Riukojetna covered the  
544 uppermost lake until 8.1 ka after which it retreated and thinned. However, although the ice cap perhaps



545 remained smaller than today until shortly before 4.8 ka, fine silt and clay laminations indicate that the  
546 glacier persisted and produced sediment. This in itself is quite remarkable, and contrary to some  
547 previously widely held belief of Riukojietna demise (Karlén, 1988) and more broadly Scandinavian  
548 glacier demise (e.g., Nesje, 2009) during the Holocene, that a low-elevation ice cap persisted and  
549 produced sediments throughout the HTM. How did the warming climate of the HTM adjust to sustain this  
550 ice cap and allowed it to produce glacial flour?

551 Temperature reconstructions based on vegetation proxies such as tree-line shifts and pollen composition  
552 indicate that summer temperatures were already relatively high in the early Holocene (9.5-8.5 cal ka BP;  
553 Karlén, 1976; Seppä and Birks, 2001; Kullman and Öberg, 2015) and during the HTM (Larocca and  
554 Axford, 2022). Given the paleo-record evidence for higher summer temperatures, we infer that  
555 Riukojietna remained in an advanced position until 8.1 ka and then persisted throughout the HTM  
556 because accumulation season precipitation was high enough to sustain the glacier. Indeed, a switch to a  
557 wetter post 8.1 ka Arctic (Thomas et al., 2018) and a wet early Holocene climate for Scandinavia, inferred  
558 from pollen and lake isotope records, may have resulted from a shifting dominance of moist North  
559 Atlantic air masses over Arctic air masses (Seppä and Hammarlund, 2000; Seppä and Birks, 2001;  
560 Shemesh et al., 2001) and a diminished influence of the deglaciating FIS. The reason for this switch may  
561 reside in warmer Arctic seas delivering more moisture and hemispheric warming driving increased  
562 poleward moisture transport (Thomas et al., 2018). Lake records showing surviving and even advancing  
563 glaciers during the early Holocene come from Austre Okstindbreen in northern Norway (Bakke et al.,  
564 2010). With summer temperatures higher-than-today and winters wetter-than-today characterizing the  
565 HTM, Riukojietna would have had a larger mass throughput which means, with a configuration as small  
566 as or even smaller than today, higher ice flow velocities and more favorable conditions for wet-based ice  
567 and bedrock erosion or sediment evacuation.

568 A reduction in ablation season temperature (Seppä and Birks, 2001), may have promoted a brief advance  
569 or ice cap reactivation recorded in Pajep Luoktejaure sediments before 5.0 ka. A nearby glacier also  
570 advanced around this time (Rosqvist et al., 2004) and so did several glaciers in northern Norway (Bakke  
571 et al., 2010; Wittmeier et al., 2015; Jansen et al., 2016).

572 Thinning and retreat of Riukojietna is implied by the cessation of glacial sediments into Pajep  
573 Luoktejaure after 4.8 cal ka BP. Subglacial erosion must then have been inhibited under a thin and cold-  
574 based ice cap, until, perhaps, disappearance. Because low ablation season temperatures have been inferred  
575 from vegetation proxies (Seppä and Birks, 2001) relative to HTM, we suggest that the ice cap primarily  
576 responded to a reduction in winter snow accumulation. We cannot currently preclude the complete demise  
577 of Riukojietna without further studies of upstream lakes 1009 and 1063. We currently favor a retracted ice



578 cap configuration over full deglaciation because glacier model studies (e.g., Stroeven, 1996) clearly show  
579 that it requires more climate deterioration to grow an ice cap anew than to expand a remnant ice cap  
580 (hysteresis).

581 The ice cap reactivated and advanced again after 1.8 cal ka BP, as evidenced by laminated glacial  
582 sediments in Pajep Luoktejaure and historical evidence. The advance was likely triggered by a  
583 simultaneous lowering of ablation season temperatures and an increase in accumulation season  
584 precipitation. The increase in winter precipitation likely also prompted glaciers on the Lyngen Peninsula  
585 in northern Norway to advance at 1.8 cal ka BP (Bakke et al., 2005). A pronounced cooling starting at ca.  
586 2 cal ka BP has been inferred from carbonate and diatom oxygen isotope records from several lakes in the  
587 area (Shemesh et al., 2001; Rosqvist et al., 2004, 2007). Evidence of a cooling at this time also comes  
588 from other parts of the Arctic (Kaufmann et al., 2009; Larocca and Axford, 2022) and the Northern  
589 Hemisphere (Solomina et al., 2016). Riukojietna remained in a relatively advanced position until the end  
590 of the LIA (Pohjola et al., 2005) after which it retreated to its current state.

## 591 **6 Conclusions**

592 In this paper we reconstruct glacier extent during the Holocene by means of cosmogenic nuclide  
593 modeling, thus integrating uncertainties from two traditional glacier reconstruction techniques. We apply  
594 this approach to Riukojietna, a small, low-altitude, low-gradient ice cap in northern Sweden, by  
595 combining direct evidence for ice-free conditions and ice-burial durations from cosmogenic nuclide  
596 chronometry (*in situ*  $^{14}\text{C}$ ,  $^{10}\text{Be}$ ,  $^{26}\text{Al}$ ) and indirect evidence of glacial extent and activity derived from  
597 proglacial lacustrine records. This allows us to present the strongest case yet for a full Holocene glacial  
598 history of a Swedish glacier, and evaluate its sensitivity to climate change. An increase in winter  
599 precipitation during the early Holocene allowed the ice cap to be relatively large until 8.1 ka and to persist  
600 through peak Holocene warming before a possible brief reactivation prior to 5.0 cal ka BP. Drier  
601 conditions in the late Holocene forced its retreat to a configuration smaller than today until colder  
602 conditions during the last two millennia allowed the glacier to advance to its 8.1 ka position at the end of  
603 the LIA.

604 Modeling shows that the glacier history derived from lake sediment studies, given appropriate  
605 assumptions, yields cosmogenic nuclide inventories showing that Riukojietna was as small or smaller  
606 than today during earlier parts of the Holocene, that including subglacial erosion can improve model  
607 results, and that even for such a low-elevation ice cap the likelihood that it persisted throughout the  
608 Holocene is larger than that it disappeared (but this remains to be conclusively demonstrated). This last  
609 inference has ramifications for other higher-seated glaciers in Sweden and northern Scandinavia, where



610 some paleoenvironmental studies have previously inferred the Holocene demise and regrowth of these  
611 glaciers, but where considerations of cold-based conditions and application of cosmogenic nuclide studies  
612 could potentially reveal complete Holocene ice-occupational histories.

### 613 **Declaration of competing interests**

614 The authors declare that they have no competing interests.

### 615 **Acknowledgements**

616 Funding for the research was provided by “Stiftelsen Carl Mannerfelts fond”, “Göran Gustafssons Stiftelse,  
617 Lappland”, and the “Albert and Maria Bergströms Stiftelse”. Funding for this research was also provided by US  
618 National Science Foundation grants EAR-1560658 and EAR-2300559. We thank Mikael Amlert for help during  
619 field collection, Adrian Singleton (Purdue University) for initial sample processing, and Simon Larsson (Stockholm  
620 University) for assistance with Rbacon (Figs 4c and S1). JLA was supported by a Wenner-Gren Foundations  
621 Stipend.

### 622 **Author contributions**

623 This study was conceived by APS, GCR, and NAL. Sample material was collected by APS, GCR, and NAL.  
624 Cosmogenic sample preparation and analysis was done by AJK. Ice reconstructions were done by C-AW. JLA,  
625 AJK, and NAL wrote the model code. This manuscript is based on a portion of the Ph.D. dissertation of AJK. All  
626 authors contributed to the manuscript.

### 627 **Data Availability**

628 All MATLAB code will be available on GitHub for reviewers (<https://github.com/jaluan/Riukojieta/tree/for-paper>)  
629 and a permanent DOI will be available after publication.

### 630 **References**

- 631 Aa, A. R., and Sønstegeard, E.: Early-Holocene glacier fluctuations of northern Grovabreen, western Norway,  
632 Holocene, 29, 187–196, <https://doi.org/10.1177/0959683618810392>, 2019.
- 633 Andersen, J. L., Newall, J. C., Blomdin, R., Sams, S. E., Fabel, D., Koester, A. J., Lifton, N. A., Fredin, O., Caffee,  
634 M. W., Glasser, N. F., Rogozhina, I., Suganuma, Y., Harbor, J. M., and Stroeven, A. P.: Ice surface changes  
635 during recent glacial cycles along the Jutulstraumen and Penck Trough ice streams in western Dronning Maud  
636 Land, East Antarctica, Quaternary Sci. Rev., 249, 106636, <https://doi.org/10.1016/j.quascirev.2020.106636>,  
637 2020.



- 638 Andreassen, L. M., Elvehøy, H., Kjølmoen, B., and Belart, J. M. C.: Glacier change in Norway since the 1960s—an  
639 overview of mass balance, area, length and surface elevation changes, *J. Glaciol.*, 66, 313–328,  
640 <https://doi.org/10.1017/jog.2020.10>, 2020.
- 641 Andréasson, P. G., and Gee, D. G.: Bedrock geology and morphology of the Tarfala area, Kebnekaise Mts., Swedish  
642 Caledonides, *Geogr. Ann.*, 71A, 235–239, <https://doi.org/10.1080/04353676.1989.11880290>, 1989.
- 643 Bakke, J., Dahl, S. O., Paasche, Ø., Løvlie, R., and Nesje, A.: Glacier fluctuations, equilibrium-line altitudes and  
644 palaeoclimate in Lyngen, northern Norway, during the Lateglacial and Holocene, *Holocene*, 15, 518–540,  
645 <https://doi.org/10.1191/0959683605hl815rp>, 2005.
- 646 Bakke, J., Dahl, S. O., Paasche, Ø., Simonsen, J. R., Kvisvik, B., Bakke, K., and Nesje, A.: A complete record of  
647 Holocene glacier variability at Austre Okstindbreen, northern Norway: an integrated approach, *Quaternary*  
648 *Sci. Rev.*, 29, 1246–1262, <https://doi.org/10.1016/j.quascirev.2010.02.012>, 2010.
- 649 Balco, G.: Production rate calculations for cosmic-ray-muon-produced  $^{10}\text{Be}$  and  $^{26}\text{Al}$  benchmarked against  
650 geological calibration data, *Quaternary Geochronol.*, 39, 150–173,  
651 <https://doi.org/10.1016/j.quageo.2017.02.001>, 2017.
- 652 Balco, G., Stone, J. O., Lifton, N. A., and Dunai, T. J.: A complete and easily accessible means of calculating  
653 surface exposure ages or erosion rates from  $^{10}\text{Be}$  and  $^{26}\text{Al}$  measurements, *Quaternary Geochronol.*, 3, 174–  
654 195, <https://doi.org/10.1016/j.quageo.2007.12.001>, 2008.
- 655 Balco, G., Brown, N., Nichols, K., Venturelli, R. A., Adams, J., Braddock, S., Campbell, S., Goehring, B., Johnson,  
656 J. S., Rood, D. H., Wilcken, K., Hall, B., and Woodward, J.: Reversible ice sheet thinning in the Amundsen  
657 Sea Embayment during the Late Holocene, *The Cryosphere*, 17, 1787–1801, <https://doi.org/10.5194/tc-17-1787-2023>, 2023.
- 659 Barnekow, L. Holocene regional and local vegetation history and lake-level changes in the Torneträsk area, northern  
660 Sweden, *J. Paleolimnol.*, 23, 399–420, <https://doi.org/10.1023/A:1008171418429>, 2000.
- 661 Benn, D. I., and Hulton, N. R. J.: An Excel™ spreadsheet program for reconstructing the surface profile of former  
662 mountain glaciers and ice caps, *Comput. Geosci.*, 36, 605–610, <https://doi.org/10.1016/j.cageo.2009.09.016>,  
663 2010.
- 664 Bergman, S., Stephens, M. B., Andersson, J., Kathol, B., and Bergman, T.: Bedrock map of Sweden, Scale 1:1  
665 million, *Sveriges geologiska undersökning*, K 423, 2012.
- 666 Binnie, S. A., Dewald, A., Heinze, S., Voronina, E., Hein, A., Wittmann, H., von Blanckenburg, F., Hetzel, R.,  
667 Christl, M., Schaller, M., Léanni, L., ASTER Team, Hippe, K., Vockenhuber, C., Ivy-Ochs, S., Maden, C.,  
668 Fülöp, R. H., Fink, D., Wilcken, K. M., Fujioka, T., Fabel, D., Freeman, S. P. H. T., Xu, S., Fifield, L. K.,  
669 Akçar, N., Spiegel, C., and Dunai, T. J.: Preliminary results of CoQtz-N: A quartz reference material for  
670 terrestrial in-situ cosmogenic  $^{10}\text{Be}$  and  $^{26}\text{Al}$  measurements, *Nucl. Instrum. Meth. B*, 456, 203–212,  
671 <https://doi.org/10.1016/j.nimb.2019.04.073>, 2019.
- 672 Bjune, A. E., Bakke, J., Nesje, A., and Birks, H. J. B.: Holocene mean July temperature and winter precipitation in  
673 western Norway inferred from palynological and glaciological lake-sediment proxies, *Holocene*, 15, 177–189,  
674 <https://doi.org/10.1191/0959683605hl798rp>, 2005.
- 675 Blaauw, M., and Christen, J. A.: Flexible paleoclimate age-depth models using an autoregressive gamma process,  
676 *Bayesian Anal.*, 6, 457–474, <https://doi.org/10.1214/11-BA618>, 2011.



- 677 Borchers, B., Marrero, S., Balco, G., Caffee, M., Goehring, B., Lifton, N., Nishiizumi, K., Phillips, F., Schaefer, J.,  
678 and Stone, J.: Geological calibration of spallation production rates in the CRONUS-Earth project, *Quaternary*  
679 *Geochronol.*, 31, 188–198, <https://doi.org/10.1016/j.quageo.2015.01.009>, 2016.
- 680 Briner, J. P., Lifton, N. A., Miller, G. H., Refsnider, K., Anderson, R., and Finkel, R.: Using in situ cosmogenic  
681  $^{10}\text{Be}$ ,  $^{14}\text{C}$ , and  $^{26}\text{Al}$  to decipher the history of polythermal ice sheets on Baffin Island, Arctic Canada,  
682 *Quaternary Geochronol.*, 19, 4–13, <https://doi.org/10.1016/j.quageo.2012.11.005>, 2014.
- 683 Chmeleff, J., von Blanckenburg, F., Kossert, K., and Jakob, D.: Determination of the  $^{10}\text{Be}$  half-life by multicollector  
684 ICP-MS and liquid scintillation counting, *Nucl. Instrum. Meth. B*, 268, 192–199,  
685 <https://doi.org/10.1016/j.nimb.2009.09.012>, 2010.
- 686 Dunai, T. J.: *Cosmogenic Nuclides: Principles, Concepts and Applications in the Earth Surface Sciences*, Cambridge  
687 University Press, 187 p., 2010.
- 688 Dussailant, I., Hugonnet, R., Huss, M., Berthier, E., Bannwart, J., Paul, F., and Zemp, M.: Annual mass change of  
689 the world's glaciers from 1976 to 2024 by temporal downscaling of satellite data with in situ observations,  
690 *Earth Syst. Sci. Data*, 17, 1977–2006, <https://doi.org/10.5194/essd-17-1977-2025>, 2025.
- 691 Fabel, D., Stroeven, A. P., Harbor, J., Kleman, J., Elmore, D., and Fink, D.: Landscape preservation under  
692 Fennoscandian ice sheets determined from in situ produced  $^{10}\text{Be}$  and  $^{26}\text{Al}$ , *Earth Planet. Sc. Lett.*, 201, 397–  
693 406, [https://doi.org/10.1016/S0012-821X\(02\)00714-8](https://doi.org/10.1016/S0012-821X(02)00714-8), 2002.
- 694 Goehring, B. M., Schaefer, J. M., Schluechter, C., Lifton, N. A., Finkel, R. C., Jull, A. J. T., Akçar, N., and Alley, R.  
695 B.: The Rhone Glacier was smaller than today for most of the Holocene, *Geology*, 39, 679–682,  
696 <https://doi.org/10.1130/G32145.1>, 2011.
- 697 Gosse, J. C., and Phillips, F. M.: Terrestrial in situ cosmogenic nuclides: theory and application, *Quaternary Sci.*  
698 *Rev.*, 20, 1475–1560, [https://doi.org/10.1016/S0277-3791\(00\)00171-2](https://doi.org/10.1016/S0277-3791(00)00171-2), 2001.
- 699 Grove, J. M.: *The Little Ice Age*, 2nd Edition, Routledge, London, <https://doi.org/10.4324/9780203505205>, 2004.
- 700 Hippe, K., Lifton, N. A.: Calculating isotope ratios and nuclide concentrations for in situ cosmogenic  $^{14}\text{C}$  analyses,  
701 *Radiocarbon*, 56, 1167–1174, <https://doi.org/10.2458/56.17917>, 2014.
- 702 Hock, R., Rasul, G., Adler, C., Cáceres, B., Gruber, S., Hirabayashi, Y., Jackson, M., Kääb, A., Kang, S., Kutuzov,  
703 S., Milner, A., Molau, U., Morin, S., Orlove, B., and Steltzer, H.: High Mountain Areas, In Pörtner, H.-O.,  
704 Roberts, D. C., Masson-Delmotte, V., Zhai, P., Tignor, M., Poloczanska, E., Mintenbeck, K., Alegria, A.,  
705 Nicolai, M., Okem, A., Petzold, J., Rama, B., and Weyer, N. M. (Eds.): *IPCC Special Report on the Ocean*  
706 *and Cryosphere in a Changing Climate*, 131–202, 2019.
- 707 Hugonnet, R., McNabb, R., Berthier, E., Menounos, B., Nuth, C., Girod, L., Farinotti, D., Huss, M., Dusailant, I.,  
708 Brun, F., and Kääb, A.: Accelerated global glacier mass loss in the early twenty-first century, *Nature*, 592,  
709 726–731, <https://doi.org/10.1038/s41586-021-03436-z>, 2021.
- 710 Jansen, H. L., Simonsen, J. R., Dahl, S. O., Bakke, J., and Nielsen, P. R.: Holocene glacier and climate fluctuations  
711 of the maritime ice cap Høgtuvbreen, northern Norway, *Holocene*, 26, 736–755,  
712 <https://doi.org/10.1177/0959683615618265>, 2016.
- 713 Jansson, P., Rosqvist, G., and Schneider, T.: Glacier fluctuations, suspended sediment flux and glacio-lacustrine  
714 sediments, *Geogr. Ann.*, 87A, 37–50, <https://doi.org/10.1111/j.0435-3676.2005.00243.x>, 2005.



- 715 Johnson, J. S., Nichols, K. A., Goehring, B. M., Balco, G., and Schaefer, J. M.: Abrupt mid-Holocene ice loss in the  
716 western Weddell Sea Embayment of Antarctica, *Earth Planet. Sc. Lett.*, 518, 127–135,  
717 <https://doi.org/10.1016/j.epsl.2019.05.002>, 2019.
- 718 Karlén, W.: Holocene glacier and climatic variations, Kebnekaise Mountains, Swedish Lapland, *Geogr. Ann.*, 55A,  
719 29–63, <https://doi.org/10.1080/04353676.1973.11879879>, 1973.
- 720 Karlén, W.: Lacustrine sediments and tree-limit variations as indicators of Holocene climatic fluctuations in  
721 Lapland, northern Sweden, *Geogr. Ann.*, 58A, 1–34, <https://doi.org/10.1080/04353676.1976.11879921>,  
722 1976.
- 723 Karlén, W.: Lacustrine sediment studies: A technique to obtain a continuous record of Holocene glacier variations,  
724 *Geogr. Ann.*, 63A, 273–281, <https://doi.org/10.1080/04353676.1981.11880042>, 1981.
- 725 Karlén, W.: Scandinavian glacial and climate fluctuations during the Holocene, *Quaternary Sci. Rev.*, 7, 199–209,  
726 [https://doi.org/10.1016/0277-3791\(88\)90006-6](https://doi.org/10.1016/0277-3791(88)90006-6), 1988.
- 727 Karlén, W., and Denton, G. H.: Holocene glacial variations in Sarek National Park, northern Sweden, *Boreas*, 5, 25–  
728 56, <https://doi.org/10.1111/j.1502-3885.1976.tb00329.x>, 1976.
- 729 Karlén, W., Bodin, A., Kuylenstierna, J., and Naslund, J.-O.: Climate of northern Sweden during the Holocene, *J.*  
730 *Coastal Res. Spec. Issue*, 17, 49–54, 1995.
- 731 Kaufman, D. S., Schneider, D. P., McKay, N. P., Ammann, C. M., Bradley, R. S., Briffa, K. R., Miller, G. H., Otto-  
732 Bliessner, B. L., Overpeck, J. T., Vinther, B. M., Arctic Lakes 2K Project Members, Abbott, M., Axford, Y.,  
733 Bird, B., Birks, H. J. B., Bjune, A. E., Briner, J., Cook, T., Chipman, M., Francus, P., Gajewski, K.,  
734 Geirsdóttir, Á., Hu, F. S., Kutcho, B., Lamoureux, S., Loso, M., MacDonald, G., Peros, M., Porinchu, D.,  
735 Schiff, C., Seppä, H., and Thomas, E.: Recent warming reverses long-term Arctic cooling, *Science*, 325,  
736 1236–1239, <https://doi.org/10.1126/science.1173983>, 2009.
- 737 Knudsen, M. F., Egholm, D. L., and Jansen, J. D.: Time-integrating cosmogenic nuclide inventories under the  
738 influence of variable erosion, exposure, and sediment mixing, *Quaternary Geochronol.*, 51, 110–119,  
739 <https://doi.org/10.1016/j.quageo.2019.02.005>, 2019.
- 740 Koester, A. J.: Applications of in situ  $^{14}\text{C}$  to glacial landscapes in Sweden and Antarctica [PhD Dissertation]: Purdue  
741 University, 186 p., 2023.
- 742 Koester, A. J., and Lifton, N. A.: Technical note: A software framework for calculating compositionally dependent  
743 in situ  $^{14}\text{C}$  production rates, *Geochronol.*, 5, 21–33, <https://doi.org/10.5194/gchron-5-21-2023>, 2023.
- 744 Koester, A. J., and Lifton, N. A.: Corrigendum to “Technical note: A software framework for calculating  
745 compositionally dependent in situ  $^{14}\text{C}$  production rates” published in *Geochronology*, 5, 21–33, 2023,  
746 *Geochronol.*, <https://doi.org/10.5194/gchron-5-21-2023-corrigendum>, 2024.
- 747 Kohl, C. P., and Nishiizumi, K.: Chemical isolation of quartz for measurement of in-situ-produced cosmogenic  
748 nuclides, *Geochim. Cosmochim. Ac.*, 56, 3583–3587, [https://doi.org/10.1016/0016-7037\(92\)90401-4](https://doi.org/10.1016/0016-7037(92)90401-4), 1992.
- 749 Korschinek, G., Bergmaier, A., Faestermann, T., Gerstmann, U. C., Knie, K., Rugel, G., Wallner, A., Dillmann, I.,  
750 Dollinger, G., Lierse von Gostomski, Ch., Kossert, K., Maiti, M., Poutivtsev, M., and Remmert, A.: A new  
751 value for the half-life of  $^{10}\text{Be}$  by Heavy-Ion Elastic Recoil Detection and liquid scintillation counting, *Nucl.*  
752 *Instrum. Meth. B*, 268, 187–191, <https://doi.org/10.1016/j.nimb.2009.09.020>, 2010.



- 753 Kullman, L., and Öberg, L.: New aspects of high-mountain palaeobiogeography: A synthesis of data from forefields  
754 of receding glaciers and ice patches in the Tärna and Kebnekaise mountains, Swedish Lapland, ARCTIC, 68,  
755 141–152, <https://doi.org/10.14430/arctic4480>, 2015.
- 756 Larocca, L. J., and Axford, Y.: Arctic glaciers and ice caps through the Holocene: a circumpolar synthesis of lake-  
757 based reconstructions, *Clim. Past*, 18, 579–606, <https://doi.org/10.5194/cp-18-579-2022>, 2022.
- 758 Leonard, E. M.: Use of lacustrine sedimentary sequences as indicators of Holocene glacial history, Banff National  
759 Park, Alberta, Canada, *Quaternary Res.*, 26, 218–231, [https://doi.org/10.1016/0033-5894\(86\)90106-7](https://doi.org/10.1016/0033-5894(86)90106-7), 1986.
- 760 Lifton, N., Sato, T., and Dunai, T. J.: Scaling in situ cosmogenic nuclide production rates using analytical  
761 approximations to atmospheric cosmic-ray fluxes, *Earth Planet. Sc. Lett.*, 386, 149–160,  
762 <https://doi.org/10.1016/j.epsl.2013.10.052>, 2014.
- 763 Lifton, N. A., Phillips, F. M., and Cerling, T. E.: Using Lake Bonneville features to calibrate in situ cosmogenic  
764 nuclide production rates, *Developments Earth Surf. Proc.*, 20, 165–183, <https://doi.org/10.1016/B978-0-444-63590-7.00009-3>, 2016.
- 766 Lifton, N., Wilson, J., and Koester, A.: Technical note: Studying lithium metaborate fluxes and extraction protocols  
767 with a new, fully automated in situ cosmogenic  $^{14}\text{C}$  processing system at PRIME Lab, *Geochronol.*, 5, 361–  
768 375, <https://doi.org/10.5194/gchron-5-361-2023>, 2023.
- 769 Matthews, J. A., and Briffa, K. R.: The ‘Little Ice Age’: Re-evaluation of an evolving concept, *Geogr. Ann.*, 87A,  
770 17–36, <https://doi.org/10.1111/j.0435-3676.2005.00242.x>, 2005.
- 771 Matthews, J. A., and Dresser, P. Q.: Holocene glacier variation chronology of the Smørstabbtindan massif,  
772 Jotunheimen, southern Norway, and the recognition of century- to millennial-scale European Neoglacial  
773 Events, *Holocene*, 18, 181–201, <https://doi.org/10.1177/0959683607085608>, 2008.
- 774 Nesje, A.: Latest Pleistocene and Holocene alpine glacier fluctuations in Scandinavia, *Quaternary Sci. Rev.*, 28,  
775 2119–2136, <https://doi.org/10.1016/j.quascirev.2008.12.016>, 2009.
- 776 Nesje, A., Dahl, S. O., Andersson, C., and Matthews, J. A.: The lacustrine sedimentary sequence in  
777 Sygneskardvatnet, western Norway: A continuous, high-resolution record of the Jostedalbreen ice cap during  
778 the Holocene, *Quaternary Sci. Rev.*, 19, 1047–1065, [https://doi.org/10.1016/S0277-3791\(99\)00090-6](https://doi.org/10.1016/S0277-3791(99)00090-6), 2000.
- 779 Nesje, A., Bakke, J., Dahl, S. O., Lie, Ø., and Matthews, J. A.: Norwegian mountain glaciers in the past, present and  
780 future, *Glob. Planet. Change*, 60, 10–27, <https://doi.org/10.1016/j.gloplacha.2006.08.004>, 2008.
- 781 Nichols, K. A., and Goehring, B. M.: Isolation of quartz for cosmogenic in situ  $^{14}\text{C}$  analysis, *Geochronol.*, 1, 43–52,  
782 <https://doi.org/10.5194/gchron-1-43-2019>, 2019.
- 783 Nichols, K. A., Goehring, B. M., Balco, G., Johnson, J. S., Hein, A. S., and Todd, C.: New Last Glacial Maximum  
784 ice thickness constraints for the Weddell Sea Embayment, Antarctica, *The Cryosphere*, 13, 2935–2951,  
785 <https://doi.org/10.5194/tc-13-2935-2019>, 2019.
- 786 Nielsen, P. R., Balascio, N. L., Dahl, S. O., Jansen, H. L., Støren, E. W. N., and Bradley, R. S.: A high-resolution  
787 1200-year lacustrine record of glacier and climate fluctuations in Lofoten, northern Norway, *Holocene*, 26,  
788 917–934, <https://doi.org/10.1177/0959683615622551>, 2016.
- 789 Nishiizumi, K.: Preparation of  $^{26}\text{Al}$  AMS standards, *Nucl. Instrum. Meth. B*, 223–224, 388–392,  
790 <https://doi.org/10.1016/j.nimb.2004.04.075>, 2004.



- 791 Oerlemans, J.: Extracting a climate signal from 169 glacier records, *Science*, 308, 675–677,  
792 <https://doi.org/10.1126/science.1107046>, 2005.
- 793 Oerlemans, J., and Fortuin, J. P. F.: Sensitivity of glaciers and small ice caps to greenhouse warming, *Science*, 258,  
794 115–118, <https://doi.org/10.1126/science.258.5079.115>, 1992.
- 795 Oerlemans, J., Anderson, B., Hubbard, A., Huybrechts, P., Jóhannesson, T., Knap, W. H., Schmeits, M., Stroeven,  
796 A. P., van de Wal, R. S. W., Wallinga, J., and Zuo, Z.: Modelling the response of glaciers to climate warming,  
797 *Clim. Dynam.*, 14, 267–274, <https://doi.org/10.1007/s003820050222>, 1998.
- 798 Phillips, F. M., Argento, D. C., Balco, G., Caffee, M. W., Clem, J., Dunai, T. J., Finkel, R., Goehring, B., Gosse, J.  
799 C., Hudson, A. M., Jull, A. J. T., Kelly, M. A., Kurz, M., Lal, D., Lifton, N., Marrero, S. M., Nishiizumi, K.,  
800 Reedy, R. C., Schaefer, J., Stone, J. O. H., Swanson, T., and Zreda, M. G.: The CRONUS-Earth Project: A  
801 synthesis, *Quaternary Geochronol.*, 31, 119–154, <https://doi.org/10.1016/j.quageo.2015.09.006>, 2016.
- 802 Ploeg, K., and Stroeven, A. P.: History and dynamics of Fennoscandian Ice Sheet retreat, contemporary ice-dammed  
803 lake evolution, and faulting in the Torneträsk area, northwestern Sweden, *The Cryosphere*, 19, 347–373,  
804 <https://doi.org/10.5194/tc-19-347-2025>, 2025.
- 805 Pohjola, V. A., Cole-Dai, J., Rosqvist, G., Stroeven, A. P., and Thompson, L. G.: Potential to recover climatic  
806 information from Scandinavian ice cores: An example from the small ice cap Riukojietna, *Geogr. Ann.*, 87A,  
807 259–270, <https://doi.org/10.1111/j.0435-3676.2005.00257.x>, 2005.
- 808 Rand, C., and Goehring, B. M.: The distribution and magnitude of subglacial erosion on millennial timescales at  
809 Engabreen, Norway, *Ann. Glaciol.*, 60, 73–81, <https://doi.org/10.1017/aog.2019.42>, 2019.
- 810 Reimer, P. J., Austin, W. E. N., Bard, E., Bayliss, A., Blackwell, P. G., Bronk Ramsey, C., Butzin, M., Cheng, H.,  
811 Edwards, R. L., Friedrich, M., Grootes, P. M., Guilderson, T. P., Hajdas, I., Heaton, T. J., Hogg, A. G.,  
812 Hughen, K. A., Kromer, B., Manning, S. W., Muscheler, R., Palmer, J. G., Pearson, C., van der Plicht, J.,  
813 Reimer, R. W., Richards, D. A., Scott, E. M., Southon, J. R., Turney, C. S. M., Wacker, L., Adolphi, F.,  
814 Büntgen, U., Capano, M., Fahrni, S. M., Fogtmann-Schulz, A., Friedrich, R., Köhler, P., Kudsk, S., Miyake,  
815 F., Olsen, J., Reinig, F., Sakamoto, M., Sookdeo, A., and Talamo, S.: The IntCal20 Northern Hemisphere  
816 radiocarbon age calibration curve (0–55 cal kBP), *Radiocarbon*, 62, 725–757,  
817 <https://doi.org/10.1017/RDC.2020.41>, 2020.
- 818 Rosqvist, G., and Østrem, G.: The sensitivity of a small icecap to climatic fluctuations, *Geogr. Ann.*, 71A, 99–103,  
819 <https://doi.org/10.1080/04353676.1989.11880277>, 1989.
- 820 Rosqvist, G., Jonsson, C., Yam, R., Karlén, W., and Shemesh, A.: Diatom oxygen isotopes in pro-glacial lake  
821 sediments from northern Sweden: A 5000 year record of atmospheric circulation, *Quaternary Sci. Rev.*, 23,  
822 851–859, <https://doi.org/10.1016/j.quascirev.2003.06.009>, 2004.
- 823 Rosqvist, G., Leng, M., and Jonsson, C.: North Atlantic region atmospheric circulation dynamics inferred from a  
824 late-Holocene lacustrine carbonate isotope record, northern Swedish Lapland, *Holocene*, 17, 867–873,  
825 <https://doi.org/10.1177/0959683607080508>, 2007.
- 826 Røthe, T. O., Bakke, J., and Støren, E. W. N.: Glacier outburst floods reconstructed from lake sediments and their  
827 implications for Holocene variations of the plateau glacier Folgefonna in western Norway, *Boreas*, 48, 616–  
828 634, <https://doi.org/10.1111/bor.12388>, 2019.
- 829 Rounce, D. R., Hock, R., Maussion, F., Hugonnet, R., Kochtitzky, W., Huss, M., Berthier, E., Brinkerhoff, D.,  
830 Compagno, L., Copland, L., Farinotti, D., Menounos, B., and McNabb, R. W.: Global glacier change in the



- 831 21st century: every increase in temperature matters, *Science*, 379, 78–83,  
832 <https://doi.org/10.1126/science.abo1324>, 2023.
- 833 Rubensdotter, L., and Rosqvist, G.: The effect of geomorphological setting on Holocene lake sediment variability,  
834 northern Swedish Lapland, *J. Quaternary Sci.*, 18, 757–767, <https://doi.org/10.1002/jqs.800>, 2003.
- 835 Santos, G. M., Southon, J. R., Druffel-Rodriguez, K. C., Griffin, S., and Mazon, M.: Magnesium Perchlorate as an  
836 alternative water trap in AMS graphite sample preparation: A report on sample preparation at KCCAMS at the  
837 University of California, Irvine, *Radiocarbon*, 46, 165–174, <https://doi.org/10.1017/S0033822200039485>,  
838 2004.
- 839 Santos, G. M., Moore, R. B., Southon, J. R., Griffin, S., Hinger, E., and Zhang, D.: AMS <sup>14</sup>C sample preparation at  
840 the KCCAMS/UCI Facility: Status report and performance of small samples, *Radiocarbon*, 49, 255–269,  
841 <https://doi.org/10.1017/S0033822200042181>, 2007.
- 842 Schimmelpfennig, I., Schaefer, J. M., Lamp, J., Godard, V., Schwartz, R., Bard, E., Tuna, T., Akçar, N., Schlüchter,  
843 C., Zimmerman, S., and ASTER Team: Glacier response to Holocene warmth inferred from in situ <sup>10</sup>Be and  
844 <sup>14</sup>C bedrock analyses in Steingletscher’s forefield (central Swiss Alps), *Clim. Past*, 18, 23–44,  
845 <https://doi.org/10.5194/cp-2021-110>, 2022.
- 846 Schneider, T., and Bronge, C.: Suspended sediment transport in the Storglaciären drainage basin, *Geogr. Ann.*, 78A,  
847 155–161, <https://doi.org/10.1080/04353676.1996.11880461>, 1996.
- 848 Seppä, H., and Birks, H. J. B.: July mean temperature and annual precipitation trends during the Holocene in the  
849 Fennoscandian tree-line area: pollen-based climate reconstructions, *Holocene*, 11, 527–539,  
850 <https://doi.org/10.1191/095968301680223486>, 2001.
- 851 Seppä, H., and Hammarlund, D.: Pollen-stratigraphical evidence of Holocene hydrological change in northern  
852 Fennoscandia supported by independent isotopic data, *J. Paleolimnol.*, 24, 69–79,  
853 <https://doi.org/10.1023/A:1008169800682>, 2000.
- 854 Seppä, H., Hammarlund, D., and Antonsson, K.: Low-frequency and high-frequency changes in temperature and  
855 effective humidity during the Holocene in south-central Sweden: Implications for atmospheric and oceanic  
856 forcings of climate, *Clim. Dynam.*, 25, 285–297, <https://doi.org/10.1007/s00382-005-0024-5>, 2005.
- 857 Shemesh, A., Rosqvist, G., Rietti-Shati, M., Rubensdotter, L., Bigler, C., Yam, R., and Karlén, W.: Holocene  
858 climatic change in Swedish Lapland inferred from an oxygen-isotope record of lacustrine biogenic silica,  
859 *Holocene*, 11, 447–454, <https://doi.org/10.1191/095968301678302887>, 2001.
- 860 Sjögren, P., and Damm, C.: Holocene vegetation change in northernmost Fennoscandia and the impact on  
861 prehistoric foragers 12 000–2000 cal. a BP – A review, *Boreas*, 48, 20–35, <https://doi.org/10.1111/bor.12344>,  
862 2019.
- 863 Sjögren, P. J. E.: An overview of Holocene climate reconstructions in northernmost Fennoscandia, *Septentrio*  
864 *Reports* 3, 31 p. <https://doi.org/10.7557/7.5747>, 2021.
- 865 Solomina, O. N., Bradley, R. S., Jomelli, V., Geirsdottir, A., Kaufman, D. S., Koch, J., McKay, N. P., Masiokas, M.,  
866 Miller, G., Nesje, A., Nicolussi, K., Owen, L. A., Putnam, A. E., Wanner, H., Wiles, G., and Yang, B.: Glacier  
867 fluctuations during the past 2000 years, *Quaternary Sci. Rev.*, 149, 61–90,  
868 <https://doi.org/10.1016/j.quascirev.2016.04.008>, 2016.



- 869 Stroeven, A. P.: The robustness of one-dimensional time dependent ice-flow models: A case study from  
870 Storglaciären, northern Sweden, *Geogr. Ann.*, 78A, 133–146,  
871 <https://doi.org/10.1080/04353676.1996.11880459>, 1996.
- 872 Stroeven, A. P., Fabel, D., Harbor, J., Hättestrand, C., and Kleman, J.: Quantifying the erosional impact of the  
873 Fennoscandian ice sheet in the Torneträsk–Narvik corridor, northern Sweden, based on cosmogenic  
874 radionuclide data, *Geogr. Ann.*, 84A, 275–287, <https://doi.org/10.1111/j.0435-3676.2002.00182.x>, 2002.
- 875 Stroeven, A. P., Hättestrand, C., Kleman, J., Heyman, J., Fabel, D., Fredin, O., Goodfellow, B. W., Harbor, J. M.,  
876 Jansen, J. D., Olsen, L., Caffee, M. W., Fink, D., Lundqvist, J., Rosqvist, G. C., Strömberg, B., and Jansson,  
877 K. N.: Deglaciation of Fennoscandia, *Quaternary Sci. Rev.*, 147, 91–121,  
878 <https://doi.org/10.1016/j.quascirev.2015.09.016>, 2016.
- 879 Stuiver, M., and Reimer, P. J.: Extended  $^{14}\text{C}$  data base and revised CALIB 3.0  $^{14}\text{C}$  age calibration program,  
880 *Radiocarbon*, 35, 215–230, <https://doi.org/10.1017/S0033822200013904>, 1993.
- 881 Svenonius, F.: Studien über den Kårso- und die Kebnegletscher nebst Notizen über andere Gletscher im  
882 Jukkasjärvigebirge, Part 1 of Die Gletscher Schwedens im Jahre 1908, Sveriges geologiska undersökning,  
883 serie Ca, 5, 1910.
- 884 Thomas, E. K., Castañeda, I. S., McKay, N. P., Briner, J. P., Salacup, J. M., Nguyen, K. Q., and Schweinsberg, A.  
885 D.: A wetter Arctic coincident with hemispheric warming 8,000 years ago, *Geoph. Res. Lett.*, 45, 10637–  
886 10647, <https://doi.org/10.1029/2018GL079517>, 2018.
- 887 Wahlström, C.-A.: A century of volume reduction of a small ice cap; Riukojietna northern Sweden, Unpublished  
888 MSc Thesis, Stockholm University, 2016.
- 889 Wastegård, S.: The Holocene of Sweden – a review, *GFF*, 144, 126–149,  
890 <https://doi.org/10.1080/11035897.2022.2086290>, 2022.
- 891 WGMS: Fluctuations of Glacier (FoG) Database, World Glacier Monitoring Service (WGMS), Zurich, Switzerland,  
892 <https://doi.org/10.5904/wgms-fog-2025-02b>, 2025.
- 893 Wirsig, C., Ivy-Ochs, S., Akçar, N., Lupker, M., Hippe, K., Wacker, L., Vockenhuber, C., and Schlüchter, C.:  
894 Combined cosmogenic  $^{10}\text{Be}$ , in situ  $^{14}\text{C}$  and  $^{36}\text{Cl}$  concentrations constrain Holocene history and erosion depth  
895 of Grueben glacier (CH), *Swiss J. Geosci.*, 109, 379–388, <https://doi.org/10.1007/s00015-016-0227-2>, 2016.
- 896 Wittmeier, H. E., Bakke, J., Vasskog, K., and Trachsel, M.: Reconstructing Holocene glacier activity at  
897 Langfjordjøkelen, Arctic Norway, using multi-proxy fingerprinting of distal glacier-fed lake sediments,  
898 *Quaternary Sci. Rev.*, 114, 78–99, <https://doi.org/10.1016/j.quascirev.2015.02.007>, 2015.
- 899 Young, N. E., Schaefer, J. M., Goehring, B., Lifton, N., Schimmelpennig, I., and Briner, J. P.: West Greenland and  
900 global in situ  $^{14}\text{C}$  production-rate calibrations. *J. Quaternary Sci.*, 29, 401–406,  
901 <https://doi.org/10.1002/jqs.2717>, 2014.
- 902 Young, N. E., Lesnek, A. J., Cuzzzone, J. K., Briner, J. P., Badgeley, J. A., Balter-Kennedy, A., Graham, B. L.,  
903 Cluett, A., Lamp, J. L., Schwartz, R., Tuna, T., Bard, E., Caffee, M. W., Zimmerman, S. R. H., and Schaefer,  
904 J. M.: In situ cosmogenic  $^{10}\text{Be}$ – $^{14}\text{C}$ – $^{26}\text{Al}$  measurements from recently deglaciated bedrock as a new tool to  
905 decipher changes in Greenland Ice Sheet size, *Clim. Past*, 17, 419–450, [https://doi.org/10.5194/cp-17-419-](https://doi.org/10.5194/cp-17-419-2021)  
906 [2021](https://doi.org/10.5194/cp-17-419-2021), 2021.

907